ISSN 0915-633X

NATIONAL INSTITUTE FOR FUSION SCIENCE

Helium I Line Intensity Ratios in a Plasma for the Diagnostics of Fusion Edge Plasmas

S. Sasaki, S. Takamura, S. Masuzaki, S. Watanabe,
T. Kato, K. Kadota

(Received - Jan. 6, 1995)

NIFS-346 Mar. 1995

RESEARCH REPORT
NIFS Series

NAGOYA, JAPAN

Helium I line intensity ratios in a plasma for the diagnostics of fusion edge plasmas

S. Sasaki *

Advanced Engineering Group, Keihin Product Operations, Toshiba Corporation, Suehiro-cho, Tsurumi-ku, Yokohama 230, Japan

S. Takamura, S. Masuzaki, and S. Watanabe

Department of Energy Engineering and Science, Nagoya University, Nagoya 464-01, Japan

T. Kato

National Institute for Fusion Science, Nagoya 464-01, Japan

K. Kadota

Plasma Science Center, Nagoya University, Nagoya 464-01, Japan

Electron temperature and density are measured, and the hot electrons in a plasma are investigated using the He I line intensity ratios in the NAGDIS-I linear device (Nagoya University Divertor Simulator) [S. Masuzaki, and S. Takamura, Jpn. J. Appl. Phys. **29,** 2835, (1990).]. He I line intensity ratios have been calculated with the collisional radiative model using new atomic data allowing for the presence of hot electrons, and summarized for the electron temperature and density measurements especially for the edge or divertor plasmas in the fusion device.

(PACS numbers: 52.70, 34.80.D, 50.20.H, 07.20.D)

Keyword: Helium I line intensity ratios, T_e and n_e measurements, hot electrons, fusion edge plasma, collisional radiative model.

---

*E-mail address: sasaki@kaiki.keihin.toshiba.co.jp

I. INTRODUCTION

Study of edge plasma and especially divertor plasma is one of the urgent and crucial issues in the nuclear fusion research. An active spectroscopic method, which utilizes atomic beams injected into plasma, is a promising technique for the space- and time- resolved electron density, n_e, and temperature, T_e, measurements in the fusion edge plasmas [1–3]. As a probe atom, helium has various advantages such as well-known atomic data, strong visible lines, and an intrinsic species in the fusion burning plasma. The T_e measurement using He I line intensity ratio, 492.2 nm / 471.3 nm, was proposed by Cunningham [4], and has been applied for plasma diagnostics with various discussions and improvements [5–11]. Recently n_e measurement using 667.8 nm / 728.1 nm and 501.4 nm / 504.8 nm line intensity ratios is proposed and applied in TEXTOR tokamak [10], and PSI-1 linear device [11].

In the present work, T_e and n_e measurements using He I line intensity ratios are improved to extend to high density fusion edge plasmas which sometimes contain hot electrons. The line intensity ratios are obtained from "effective emission rate coefficients", $C_{em}^{eff}(\lambda)$'s, based on the collisional radiative (C.R.) model including the excited states with principal quantum number up to 20 [12]. New recommended cross section data represented in analytic expressions are employed for the calculation of the $C_{em}^{eff}(\lambda)$ [13,14].

The T_e and n_e measurements are demonstrated in the helium discharge of the NAGDIS-I linear device [15,16]. In the low density plasma ($n_e \approx 10^{11}$ cm^{-3}), T_e measurement and the investigation of hot electron are performed. The hot electrons, which are often produced in the RF (radio frequency) heated plasmas [17], would modify the plasma edge properties such as sheath potential [18]. An effect of resonance scattering on 501.6 nm (3^1P - 2^1S), which is attractive both for T_e and n_e measurements, is discussed using the optical escape factor [19,20], and compared to the experimental result. The simultaneous n_e and T_e (T_{eh}) measurements are demonstrated in the high density plasma ($n_e = 10^{11}$ - 10^{13} cm^{-3}), which corresponds to the n_e of fusion edge plasma.

An "effective ionization rate coefficient", S^{eff}, in the C.R. model is presented for the

application of beam probe spectroscopy. The $C_{em}^{eff}(\lambda)$'s and S^{eff} of helium atom are important quantities for the investigation of the "helium ash" in the divertor plasma in the fusion device. So far, the $C_{em}^{eff}(\lambda)$'s and S^{eff} of carbon atom, which is also an important impurity specie, have been discussed and summarized elsewhere [21].

II. PRINCIPLE OF THE METHOD

A. Effective emission rate coefficients in the C.R. model

The effective emission rate coefficient $C_{em}^{eff}(\lambda)$ is obtained by the numerical code developed by Fujimoto [12], with substituting new excitation rate coefficient data for the excited states with principal quantum number up to 7 [14]. Energy level diagram of He atom considered in this work is shown in Fig. 1. We calculate the line intensities of 504.8 nm (4^1S - 2^1P), 501.6 nm (3^1P - 2^1S), 492.2 nm (4^1D - 2^1P), and 471.3 nm (4^3S - 2^3P), whose wavelengths are close each other. In the finite density plasmas, ionization and excitation/de-excitation from the excited states cannot be neglected. In the C.R. model, the rate equation of the population density $n(i)$ under the ionizing plasma condition is expressed as,

$$\frac{dn(i)}{dt} = \left(n_e \sum_{j \neq i} C_{ji} n(j) + \sum_{j>i} A_{ji} n(j) \right) - \left(n_e \sum_{j \neq i} C_{ij} n(i) + \sum_{j<i} A_{ij} n(i) \right) - n_e S_i n(i) = 0, \quad (1)$$

where A_{ij}, C_{ij} and S_i are the transition probability, the excitation/de-excitation rate coefficient from (i) to (j), and the ionization rate coefficient from (i). Here, plasma and working gas are assumed to be optically thin. The $n(i)$ is obtained from the set of simultaneous equations. The $C_{em}^{eff}(\lambda)$ [cm^3/s] for the line with wavelength λ ($i \rightarrow j$ transition) is defined as,

$$C_{em}^{eff}(\lambda) = \frac{n(i)A_{ij}}{n_e \sum_k n(k)} = \frac{n(i)A_{ij}}{n_e n_{He}}, \quad (2)$$

where n_{He} is the density of helium atoms.

Figure 2 (a) shows T_e dependence of $C_{em}^{eff}(\lambda)$ at the low density limit (n_e = 1 cm^{-3}). In such a low density plasma, $C_{em}^{eff}(\lambda)$ is close to the value in the corona model. The

C_{em}^{eff}(501.6 nm) increases toward higher T_e up to 200 eV because 1^1S - 3^1P excitation bears the characteristics of an allowed transition. Since the excitations for the 504.8 nm and 492.2 nm lines are optically forbidden transitions, the $C_{em}^{eff}(\lambda)$'s for these lines decrease toward higher T_e. For the triplet line, C_{em}^{eff}(471.3 nm), rapidly decreases toward higher T_e because of its spin change forbidden nature.

Figure 2 (b) shows the n_e dependences of $C_{em}^{eff}(\lambda)$'s at T_e = 20 eV. The $C_{em}^{eff}(\lambda)$'s are slightly larger than the emission rate coefficients in the corona model within a factor of 10 % even in the low n_e plasma, since the cascade contribution is neglected in the corona model. The n_e dependences of $C_{em}^{eff}(\lambda)$'s for singlet and triplet lines show different features. For the singlet lines, $C_{em}^{eff}(\lambda)$'s for 504.8 nm, 501.6 nm and 492.2 nm have almost constant values in $n_e \leq 10^{10}$, 10^{13} and 10^{11} cm^{-3}. respectively. In the higher n_e plasmas. $C_{em}^{eff}(\lambda)$'s decrease as n_e increases because $n(i)$'s are saturated to n_e, which comes from frequent electron collisions on the excited states. For the triplet line, the C_{em}^{eff}(471.3 nm) slightly increases in an intermediate n_e plasma, $10^4 \leq n_e \leq 10^{11}$ cm^{-3}, because of the increase of 2^3S metastable state population. In the higher n_e plasma, the frequent electron collisions makes $n(i)$ saturated to n_e resulting in the decrease of C_{em}^{eff}(471.3 nm).

The accuracy of $C_{em}^{eff}(\lambda)$ depends on the atomic data. The A_{ij} has a good accuracy less than a factor of 5 %. The accuracy of C_{ij} is estimated to be within a factor of 20 % for T_e $\leq$ 50 eV with including the analytical fitting error [13,14]. For $T_e \geq$ 50 eV. C_{ij} has higher accuracy because of less uncertainty of σ_{ij} for high electron impact energy especially for the allowed excitation.

B. Electron temperature and density measurements using line intensity ratios

The line intensity ratio $R^{eff}(\lambda_1 \ / \ \lambda_2)$ is obtained as, $R^{eff}(\lambda_1/\lambda_2) = C_{em}^{eff}(\lambda_1)/C_{em}^{eff}(\lambda_2)$, by assuming the constant sensitivity of the optical detection system for λ_1 and λ_2. Figure 3 shows the $R^{eff}(\lambda_1/\lambda_2)$'s for several singlet-triplet line pairs at the low density limit (n_e = 1 cm^{-3}). The singlet-triplet line pairs are suitable for T_e measurement because of strong

T_e dependence of $R^{eff}(\lambda_1/\lambda_2)$, coming from the different T_e dependences of $C_{em}(\lambda)$'s. In such low density plasmas, $R^{eff}(\lambda_1/\lambda_2)$ is close to the value in the corona model. The Cunningham's result of 492.2 nm / 471.3 nm in the corona model is compared to the present work in Fig. 3 [4], which has a discrepancy about a factor of two. His result is based on the experimental cross section data, where an error in its absolute-intensity calibration has been pointed out [5].

Figure 4 (a) shows T_e dependence $R^{eff}(\lambda_1/\lambda_2)$'s for singlet-triplet line pair of at $n_e = 10^{12}\text{cm}^{-3}$ corresponding to the n_e in the fusion edge plasmas. In such a high n_e plasma, $R^{eff}(\lambda_1/\lambda_2)$'s in the high n_e plasma have a large difference to those in the low n_e plasma. The n_e dependences of $R^{eff}(\lambda_1/\lambda_2)$'s for these line pairs are shown in Fig. 4 (b). The line intensity ratios in the corona model are compared to $R^{eff}(\lambda_1/\lambda_2)$'s in this figure, which coincide to $R^{eff}(\lambda_1/\lambda_2)$'s within a factor of 10 % in the low n_e region, $n_e \leq 10^4$ cm^{-3}. In the intermediate n_e plasma, $10^4 \leq n_e \leq 10^{11}$ cm^{-3}, the $R^{eff}(\lambda_1/\lambda_2)$'s for these line pairs are small compared to those in the low n_e plasma because of the increase of C^{eff}_{em}(471.3 nm) as shown in Fig. 2 (b). In the high n_e plasma with $n_e \geq 10^{11}$ - 10^{12} cm^{-3}, $R^{eff}(\lambda_1/\lambda_2)$'s have strong n_e dependences. The R^{eff}(501.6 nm / 471.3 nm) has a strong n_e dependence in $n_e \geq 10^{11}$ cm^{-3}, because of the different n_e dependences of C^{eff}_{em}(501.6 nm) and C^{eff}_{em}(471.3 nm), 2 (b). The R^{eff}(504.8 nm / 471.3 nm) is attractive for T_e measurement in the fusion edge plasmas with $n_e \approx 10^{11}$ - 10^{14} cm^{-3} because of its strong T_e dependence and relatively weak n_e dependences.

For the purpose of n_e measurement, strong n_e and weak T_e dependences of $R^{eff}(\lambda_1/\lambda_2)$ are desired. Figure 5 shows $R^{eff}(\lambda_1/\lambda_2)$'s for the singlet-singlet line pairs, which are suitable for n_e measurement. By using the strong n_e dependence of $R^{eff}(\lambda_1/\lambda_2)$, n_e measurement is available for $n_e \geq 10^{11}$ cm^{-3}. However, we should note only 10 % of the experimental error of the line intensity ratio results in the error of n_e as much as a factor of two. The result of Behrendt for R^{eff}(501.6 nm / 504.8 nm) is compared to the present work in Fig. 5 (b) [11], which shows a discrepancy within 50 %. This may come from the different atomic data and the less number of excited states included in the model (principal quantum number $\leq$

5). The weak T_e dependences of $R^{eff}(\lambda_1/\lambda_2)$'s for these singlet line pairs, Fig. 5, suggest that the ambiguity of T_e does not result in the serious error in the reproduced n_e. On the contrary, the strong n_e dependences of $R^{eff}(\lambda_1/\lambda_2)$'s for the singlet-triplet line pairs, Fig. 4(b), means we must know n_e for the T_e measurement. Therefore, n_e and T_e are alternatively determined by iterations from the singlet-singlet and singlet-triplet line pairs by using the initial value of n_e determined from the singlet-singlet one.

The reliability of $R^{eff}(\lambda_1/\lambda_2)$ depends both on the accuracy of C_{ij}'s and the C.R. model. In the plasmas with $n_e \leq 10^{11}$ cm^{-3} for singlet lines and $n_e \leq 10^{11}$ cm^{-3} for triplet lines, C_{1i}'s are important since the accuracy of $C^{eff}_{em}(\lambda)$ is dominantly determined by C_{1i}'s. However in the higher n_e plasma, the reliability of the C.R. model is important. It may depend on the atomic processes and the number of atomic levels included in the model. The number of the excited states (principal quantum number ≤ 20) is considered to be sufficient. The resonance scattering, which enlarges the population densities of n^1P excited states, should be considered in the plasma with high base pressure of He gas.

C. Effects of hot electrons on the line intensity ratio

Sometimes an electron velocity distribution function, $f(v_e)$, is not represented by a Maxwellian, but has a hot (tail) component. Such is the often case for the RF heated plasmas. We approximate $f(v_e)$ of the hot component to be a Maxwellian with high T_e. Then, $f(v_e)$ is expressed as a superposition of two Maxwellian distribution functions for cold and hot components, i.e. $f_c(v_e)$ with electron temperature of T_{ec}, and $f_h(v_e)$ with T_{eh}:

$$f(v_e) = (1-\alpha) f_c(v_e) + \alpha f_h(v_e), \tag{3}$$

where α is the abundance of the hot component, defined as $\alpha = n_{eh}/n_e$, with n_{eh} the electron density of the hot component. Then, C_{ij} is expressed as,

$$C_{ij} = \int_0^\infty \sigma_{ij} v_e f(v_e) 4\pi v_e^2 dv_e, = (1-\alpha) C_{ij}(T_{ec}) + \alpha C_{ij}(T_{eh}), \tag{4}$$

with σ_{ij} the excitation/de-excitation cross section. The $C_{ij}(T_{ec})$ and $C_{ij}(T_{ch})$ are the C_{ij} at T_{ec} and T_{eh}, respectively.

The R^{eff}(492.2 nm / 471.3 nm) in the presence of hot electrons with T_{eh} = 20 eV and 40 eV at $n_e = 10^{11}\text{cm}^{-3}$ is shown in Fig. 6 (a). This figure shows that the presence of hot electrons gives rise to a substantial modification of the line intensity ratio. The $R^{eff}(\lambda_1/\lambda_2)$ at low T_{ec}, where $(1-\alpha)C_{ij}(T_{ec}) \ll \alpha C_{ij}(T_{eh})$, is rather close to the value in the mono electron temperature plasma with T_{eh}. The n_e dependence of R^{eff}(492.2 nm / 471.3 nm) in the presence of hot electrons with T_{eh} = 40 eV and α = 10 % is shown in Fig. 6(b). The line intensity ratio in the corona model is also shown for comparison, which is very close to the value of R^{eff}(492.2 nm / 471.3 nm) at $n_e = 1\ \text{cm}^{-3}$.

III. EXPERIMENTAL RESULT

NAGDIS-I is a linear plasma device with a PIG type discharge using a LaB_6 hot cathode, operated at the axial magnetic field of $\leq$ 0.15 T [15]. The vacuum vessel has a column length of 250 cm and a radius of 13.8 cm. The plasma has T_e and n_e profiles in a trapezoid shape with a diameter of $\approx$10 cm in FWHM. The optical detection system consists of a lens, an optical fiber, a monochromator, and a photomultiplier. The sensitivity of the optical system is almost constant over the wavelengths of 504.8 nm, 501.6 nm, 492.2 nm and 471.3 nm. These line emissions are observed through a chord passing the plasma center. A numerical simulation is performed to compare the observed line intensity ratios as chord averaged values and the intensity ratios in the plasma center. Because of the large plasma column and the low n_e in the edge region, the observed line intensity ratio can be approximated as that in the plasma center. The plasma parameters T_{ec}, T_{eh}, and α at the plasma center, are measured by the Langmuir probe. The T_e measurement and the investigation of the hot electron are performed in the low density plasma ($n_e \approx 10^{11}\ \text{cm}^{-3}$), where the n_e dependences of $R^{eff}(\lambda_1/\lambda_2)$'s are weak. The simultaneous n_e and T_e (T_{eh}) measurements are performed in the high density plasmas ($n_e = 10^{11}$ - $10^{13}\ \text{cm}^{-3}$).

A. Electron temperature measurement and investigation of hot electrons

The electron temperature and the abundance of hot electrons are varied by the filling gas pressure in the "low n_e- experiment". The ion gauge shows the pressure in the vacuum vessel without the discharge is several 10^{-4} Torr. Since the pressure gauge does not represent a real value during the discharge because of the plasma pumping effect, the flow rate of the filling He gas is used as an indication of the pressure. The discharge voltage V_d is regulated to maintain a fixed discharge current at $I_d = 10$ A. The V_d in the low gas pressure is ≈ 180 V and that for high pressure is ≈ 100 V as shown in Fig. 7 (a). This figure also shows n_e measured by the Langmuir probe, n_e(L.P.). The value of $n_e \approx 1 \times 10^{11}$ cm^{-3} is considered as the upper limit where the corona model is valid (except for the triplet lines).

The electron temperatures obtained by the Langmuir probe and by the He I line intensity ratio (He I method) are compared in Fig. 7 (b). Observed line intensities and those ratios, 492.2 nm / 471.3 nm and 501.6 nm / 492.2 nm, are shown in Fig. 8. In this condition, the numerical simulation suggests that the observed line intensity ratios are slightly smaller than those in the plasma center by 2-3 %, which are small compared to the experimental error ($\approx \pm$ 5 %). Then, the experimental error of T_e in the He I method is within 3 eV. In the low pressure condition ($\leq$ 10 ccm), the Langmuir probe result shows that the plasma has a mono- electron temperature with $T_{ec} \geq$ 10 - 20 eV, though $f(v_e)$ somewhat deviates from the Maxwellian. Here, T_{ec}(L.P.) from the Langmuir probe is in good agreement with T_e(He I) from the He I method. In the high pressure condition ($\geq$ 15 ccm), hot component is separated from the cold component: T_{eh}(L.P.) $\approx$ 20 - 40 eV, $\alpha \approx 10 \pm 3$ %, T_{ec}(L.P.) $\leq$ 10 eV. Then, T_e (He I), which neglects the effect of hot electrons, is larger than T_{ec} (L.P.) as suggested by Fig. 6. In both pressure ranges, numerically obtained R^{eff}(492.2 nm / 471.3 nm) is consistent with the experimentally obtained line intensity ratio by using T_{ec}(L.P.), T_{eh}(L.P.) and $\alpha = 10 \pm 3$ % as shown in Fig. 8 (b). The determination of T_{eh} from the line intensity ratio is available if α and T_{ec} are known. The T_{eh} derived from the line intensity ratio, T_{eh}(He I), using T_{ec}(L.P.) and $\alpha = 10 \pm 3$ %, is consistent with T_{eh}(L.P.). Here, the

large deviation of T_{eh}(He I) comes from the ambiguity of α. Although the quantitative measurements of T_{eh} and α are difficult, the He I method can show the evidence of the existence of hot electrons if we know T_{ec}. It is often the case of RF experiments where the hot electrons are produced but the change of T_{ec} is small.

The line of 501.6 nm (3^1P - 2^1S) has attractive features both for T_e and n_e measurements as discussed before. In the present experiment, however, the effect of resonance scattering enlarges the 501.6 nm line intensity as shown in Fig. 8 (a), and disables T_e and n_e measurements. Here, the effect of resonance scattering is investigated using the "optical escape factor" [9,19,20] from the viewpoint of experimental applications. The optical escape factor Λ for the line center of 53.7 nm resonance line (3^1P - 1^1S) is obtained from the optical depth τ [20]. The values of Λ and τ for the He gas with temperature of 300 K are shown as functions of a column density $n_{He} \times L$ cm^{-2} in Fig. 9. Here, $\Lambda = 1$ means the He gas is optically opaque for 53.7 nm photons. In our experiment, $n_{He} \times L = 10^{14}$ cm^{-2} corresponds the He gas pressure of 2×10^{-4} Torr, where L is the radius of the vacuum vessel ($L = 13.8$ cm). The value of $\Lambda = 0.07$ at $n_e \times L = 10^{14}$ cm^{-2} means we cannot neglect this effect under the present condition. We employ a simple model including three states, i.e. the ground state (1), the 2^1S metastable state (2), and the 3^1P excited state (3). As suggested by Fig. 2(b), the corona model approximation is still valid for the singlet lines, 501.6 nm and 492.2 nm, at $n_e \approx 1 \times 10^{11}$ cm^{-3}. The rate equation for $n(3)$ using Λ is approximated as,

$$\frac{dn(3)}{dt} = n_e C_{13} n(1) - \Lambda A_{31} n(3) - A_{32} n(3) = 0. \tag{5}$$

Then, the emission rate coefficient for $\lambda = 501.6$ nm can be derived as,

$$C_{em}^{res}(501.6\text{nm}) = C_{13} \frac{A_{32}}{A_{32} + \Lambda A_{31}}. \tag{6}$$

Equation (6) explains the small value of Λ enlarges the 501.6 nm line intensity. Numerical result of 501.6 nm / 492.2 nm line intensity ratio is in a good agreement with the experimental one as shown in Fig. 8 (c). Here, $n_{He} \times L$ is assumed to be proportional to the gas flow rate. The ambiguity of n_{He} gives a large error bar on R^{eff}(501.6 nm / 492.2 nm). Further

discussions including the finite population density of the 2^1S metastable state and the effects of collisions with neutral He atoms are necessary for the detailed quantitative investigation. The small values of Λ makes the population densities of n^1P large, and this may give influence on n^1S and n^1D excited states. It is concluded, from the practical use, the effect of resonance scattering on the line of 501.6 nm can be avoided for He gas pressure below 10^{-5} Torr for $L = 13.8$ cm. A beam probe technique solves this problem by reducing the He gas density n_{He} and the column radius L.

B. Simultaneous electron density and temperature measurement

The electron density is varied by the discharge current I_d, while the flow rate of He gas is fixed at 30 ccm in the "high n_e experiment". In this condition, T_{ec} is almost constant at ≈ 5 eV, although T_{eh} and α vary by I_d. A fast scanning Langmuir probe technique is employed for n_e and T_{ec} measurements to avoid the thermal damage to the probe tip [16]. Unfortunately, T_{eh} and α cannot be measured by the probe due to the very noisy signal. The experimental result of line intensity ratios of 504.8 nm / 471.3 nm, 492.2 nm / 471.3 nm and 492.2 nm / 504.8 nm are shown in Fig. 10 (a). The former two are for T_e measurement and the latter one is for n_e measurement. Measured n_e and T_e are shown in Figs. 10 (b) and (c), respectively. In the present condition, the numerical simulation suggests that the observed line intensity ratios are smaller than those in the plasma center by within 10 % in this plasma, which is mainly due to the large spatial variation of n_e. The experimental error in the observed line intensity ratios is estimated as within $\pm$ 10 %. Only 10 % of the experimental error on the 492.2 nm / 504.8 nm line intensity ratio results in the error in the electron density, n_e(He I), as much as a factor of two. Here, n_e(He I) is obtained with the aid of T_{ec}(L.P.), T_{eh}(He I) and assuming $\alpha = 10 \pm 3$ %. The n_e obtained by the Langmuir probe, n_e(L.P.), also has a large experimental error within a factor of two. Although, both n_e(He I) and n_e(L.P.) have large experimental errors, they are consistent each other within the error bars, and have the similar I_d dependence. The T_e(He I) from the 504.8 nm /

471.3 nm and 492.2 nm / 471.3 nm line intensity ratios are large compared to T_{ec} (L.P.) because of the neglection of hot electrons. The $\pm$ 10 % of the experimental error in the line intensity ratios results in the error of reproduced T_e within 5 eV. Since T_{ec} is small at $\approx$ 5 eV, $R^{eff}(\lambda_1/\lambda_2)$ is rather close to the value at mono temperature of T_{eh} as suggested by Fig. 6. It is remarkable that T_e and T_{eh} obtained by the different line intensity ratios are close each other, although they have quite different T_e and n_e dependences. Here, the accuracy of n_e is important since $R^{eff}(\lambda_1/\lambda_2)$'s for singlet-triplet line pairs have strong n_e dependence. The T_{eh}(He I) is obtained using T_{ec}(L.P.) and assuming $\alpha = 10 \pm 3$ %, which is the Langmuir probe result at the gas flow rate of 30 ccm and the discharge current $I_d = 10$ A in the low n_e experiment. In the low I_d region ($\leq$ 15 A), T_{eh} has a value of 30 - 50 eV, while T_{eh} decreases down to 10 - 30 eV where $I_d \geq$ 15A. Here the n_e and T_e (T_{eh}) measurements using the He I line intensity ratios are demonstrated as the powerful tool for the diagnostics of fusion edge plasmas.

IV. APPLICATION AND DISCUSSION

An "effective ionization rate coefficient" S^{eff} in the C.R. model is a useful quantity for various applications. The quantity of S^{eff} is defined as,

$$S^{eff} = \frac{\sum_i n(i)S_i}{\sum_k n(k)} = \frac{\sum_i n(i)S_i}{n_{He}}. \tag{7}$$

The T_e and n_e dependences of S^{eff} are shown in Fig 11. Since S_i's (from the excited states) are much larger than S_1 (from the ground state), S^{eff} increases in the high n_e plasmas, where $n(i)$ of the excited states are large. The S^{eff} in the n_e range of $n_e = 10^4$ - 10^{14} cm^{-3}, is large compared to the value at $n_e = 1$ cm^{-3}, which comes from the n_e dependence of the metastable population densities. As n_e exceeds 10^{14} cm^{-3}, S^{eff} increases due to the ionization from the higher excited states. In the beam probe application, the spatial range of the measurement is determined by the beam penetration depth ℓ_p, which is defined as $\ell_p = v_{He}/(n_e S^{eff})$ with v_{He} the velocity of helium beam. The ℓ_p of the 300 K thermal helium

beam is estimated as 24 cm in the plasma with $T_e = 20$ eV and $n_e = 1 \times 10^{12}$ cm^{-3}. Then, the thermal He beam penetrates the scrape-off layer in the small or medium size tokamak. The S^{eff} has rather strong T_e dependence compared to the n_e dependence, which is an advantage for an another type of T_e measurement utilizing the strong T_e dependence of S^{eff} [2].

The recombination of He ions in the low T_e and/or high n_e plasmas influences on the population balances of the excited states. The population density $n(i)$ is expressed as a sum of a pure ionizing component $n(i)_{ion.}$ and a pure recombining component $n(i)_{recom.}$, i.e. $n(i) = n(i)_{ion.} + n(i)_{recom.}$. Figure 12 shows an example of $n(i)_{recom.}/n(i)$ for the 4^1D excited state obtained by the C.R. model including the recombination at $n_{He^+} \ / \ n_{He} = 0.1$. The value of $n_{He^+}/n_{He} = 0.1$ is the maximum value, which is experimentally estimated in the NAGDIS-I helium discharge. Since $T_e \approx 8$ - 20 eV in this plasma, it corresponds to the ionizing plasma. For the beam probe application, the influence of recombination can be neglected since the small amount of helium atom is injected perpendicularly to the magnetic field.

The existence of the metastable states, 2^1S and 2^3S, enlarges the relaxation times of the population densities. As suggested by the n_e dependence of $C^{eff}_{em}(\lambda)$'s, the contributions of the 2^1S on the singlet lines are relatively small compared to those of the 2^3S state for the triplet lines. Then the relaxation times for the singlet lines are considered as $\approx 1/A_{ij}$ with the order of several tens nanoseconds. Triplet lines are, however, strongly influenced by the 2^3S metastable state. Since A_{i1} for 2^3S - 1^1S transition is very small (1.7×10^{-4} s^{-1}) [22], collisional processes determine the relaxation time. The ionization is the dominant process for the population balance on the 2^3S state because of large S_i from 2^3S. The large relaxation time of 2^3S metastable state (≈ 100 μs) in the present low n_e experiment can influence the population balance of the triplet state, since the transit time of 300 K He atoms across the vessel radius (L = 13.8 cm) is the similar value (≈ 100 μs). Further discussion including the movement of He gas in the vessel and the atomic processes on the material surface is necessary for the detailed investigation.

ACKNOWLEDGMENTS

The authors are grateful to Prof. T. Fujimoto (Kyoto University) for his valuable discussions and for the numerical code of the collisional radiative model. This work was partly supported by a Grant-in-Aid of the Scientific Research from the Japan Ministry of Education, Science and Culture (JSPS Fellowship, No. 3293).

APPENDIX A: FURTHER RESULTS DERIVED FROM THE COLLISIONAL RADIATIVE MODEL

The excitation rate coefficient C_{1i} and the effective emission rate coefficient $C_{em}^{eff}(\lambda)$ are summarized. The C_{1i} to the excited states with principal quantum number up to 5 is shown in Fig. A1. The C_{1i} is numerically calculated using the cross section presented by Kato et al. [14]. The $C_{em}^{eff}(\lambda)$ is shown as a function of T_e in Fig. A2.

Line radiation power rate coefficient P_{rad}^{eff} [eVcm^3/s] is an important quantity for the investigation of power balance in the divertor plasmas. The P_{rad}^{eff} is obtained as,

$$P_{rad}^{eff} = \frac{\sum_i (n(i) \sum_{j<i} A_{ij} E_{ij})}{n_e n_{He}}, \tag{A1}$$

where E_{ij} is the energy of the line. The line radiation power per unit volume is given by $n_e P_{rad}^{eff} n_{He}$ [eVcm^{-3}/s]. Figure A3 depicts the T_e and n_e dependences of P_{rad}^{eff}. It should be noted here that this quantity is obtained for the ionizing plasma condition. Details in the line radiation power rate coefficient is described and discussed in the reference for carbon atom [21].

Two metastable states, 2^1S and 2^3S, influence on the ionization and line emission processes of helium atom. Normalized population densities, $n(i)/n_{He} = n(i)/\Sigma_k n(k)$, for the metastable states obtained by the C.R. model are shown in Fig. A4. The n_e dependences of these metastable states are consistent with the results of $C_{em}^{eff}(\lambda)$'s, S^{eff} and P_{rad}^{eff}.

APPENDIX B: APPLICATIONS

The ratio of S^{eff} / $C_{em}^{eff}(\lambda)$ is a useful quantity for the determination of beam density in the beam probe spectroscopy technique [2,3], and for the atomic impurity measurement such as carbon [21]. The ratio of S^{eff} / $C_{em}^{eff}(\lambda)$ is shown as a function of T_e in Fig. B1.

Line intensity ratios for n_e and T_e measurements are summarized for the experimental use. The figures are drawn in the n_e range of 10^{11} - 10^{14} cm^{-3} and T_e range of 5 - 50 eV. Here we present the line intensity ratios of 492.2 nm / 504.8 nm, 504.8 nm / 471.3 nm, and 492.2 nm / 471.3 nm. The former one is for n_e measurement and the latter two are for T_e measurement. The n_e dependence of R^{eff}(492.2 nm / 504.8 nm) are shown in Fig. B2 (a), which has a small T_e dependence. The n_e dependences of R^{eff}(504.8 nm / 471.3 nm) and R^{eff}(492.2 nm / 471.3 nm) are shown in Fig. B2 (b) and (c), respectively. Since these line intensity ratios have strong n_e and T_e dependences, we must know n_e for T_e measurement in the high density plasma with $n_e \geq 10^{11}$ cm^{-3}. The T_e dependences of R^{eff}(504.8 nm / 471.3 nm) and R^{eff}(492.2 nm / 471.3 nm) are summarized for T_e measurement in Fig. B3 and B4, respectively.

[1] K. Kadota, K. Tsuchida, Y. Kawasumi, and J. Fujita, Plasma Phys. **20,** 1011 (1978).

[2] A. Pospieszczyk, F. Aumayr, H. L. Bay, E. Hintz P. Leismann, Y. T. Lie, G. G. Ross, D. Rusbült, R. P. Schorn, B. Schweer, and H. Winter, J. Nucl. Mater. **162-164,** 574 (1989).

[3] S. Sasaki, Y. Uesugi, S. Takamura, H. Sanuki, and K. Kadota, Phys. Plasmas **1,** 1089 (1994).

[4] S. P. Cunningham, *Conference on Thermonuclear Reactors*, Livermore, U.S. Atomic Energy Commission Report, No.279, p.289 (1955).

[5] A. H. Gabriel, and D. W. O. Heddle, Proc. Roy. Soc. (London) **A258,** 124 (1960).

[6] C. C. Lin, and R. M. St. John, Phys. Rev. **128,** 1749 (1962).

[7] R. J. Sovie, Phys. Fluids **7,** 613 (1964).

[8] R. F. de Vries, and R. Mewe, Phys. Fluids **9,** 414 (1966).

[9] N. Brenning, J. Quant. Spectrosc. Radiat. Transfer **24,** 319 (1980).

[10] B. Schweer, G. Mank, A. Pospieszczyk, B. Brosda, B. Pohlmeyer, J. Nucl. Mater. **196-198,** 174 (1992).

[11] H. Behrendt, W. Bohmeyer, L. Dietrich, G. Fussmann, H. Greuner, H. Grote, M. Kammeyer, P. Kornejew, M. Laux, E. Pasch, *21st EPS Conference on Controlled Fusion and Plasma Physics*, Montpellier, France, III p.1328 (1994).

[12] T. Fujimoto, J. Quant. Spectrosc. Radiat. Transfer **21,** 439 (1979).

[13] F. J. de Heer, R. Hoekstra, A. E. Kingston, and H. P. Summers, Nucl. Fusion Suppl. **3,** 19 (1992).

[14] T. Kato, and R. K. Janev, Nucl. Fusion Suppl. **3,** 33 (1992).

[15] S. Masuzaki, and S. Takamura, Jpn. J. Appl. Phys. **29,** 2835 (1990).

[16] S. Masuzaki, N. Ohno, M. Takagi, and S. Takamura, Trans. IEE of Jpn. **112-A**, 913 (1992) (in Japanese).

[17] S. Takamura, A. Sato, Y. Shen, and T. Okuda, J. Nucl. Mater. **149,** 212 (1987).

[18] K. Shiraishi, and S. Takamura, J. Nucl. Mater. **176-177,** 251 (1990).

[19] T. Holstein, Phys. Rev. **72,** 1212 (1947).

[20] H. W. Drawin, and F. Emard, Beitr. Plasmaphysik **30a,** 143 (1973).

[21] S. Sasaki, Y. Ohkouchi, S. Takamura, and T. Kato, J. Phys. Soc. Jpn. **63,** 2942 (1994).

[22] C. D. Lin, W. R. Johnson, and A. Dalgarno, Phys. Rev. A, **15,** 154 (1977).

Figure captions

FIG. 1. Energy level diagram of helium atom included in C.R. model.

FIG. 2. Effective emission rate coefficients obtained by the C.R. model, $C_{em}^{eff}(\lambda)$. (a) T_e dependence of $C_{em}^{eff}(\lambda)$ at the low density limit ($n_e = 1\text{cm}^{-3}$). (b) n_e dependence of $C_{em}^{eff}(\lambda)$ at $T_e = 20$ eV.

FIG. 3. Line intensity ratios, $R^{eff}(\lambda_1/\lambda_2)$, for T_e measurement at low density limit ($n_e = 1\text{cm}^{-3}$), which are close to the values in the corona model. The result by Cunningham is shown for comparison.

FIG. 4. Line intensity ratios, $R^{eff}(\lambda_1/\lambda_2)$ for singlet-triplet line pairs, suitable for T_e measurement in the fusion edge plasmas. (a) T_e dependence of $R^{eff}(\lambda_1/\lambda_2)$ at $n_e = 10^{12}$ cm^{-3}. (b) n_e dependence of $R^{eff}(\lambda_1/\lambda_2)$ at $T_e = 20$ eV.

FIG. 5. Line intensity ratios, $R^{eff}(\lambda_1/\lambda_2)$ for singlet-singlet line pairs, suitable for n_e measurement in the fusion edge plasmas. (a) T_e dependence of $R^{eff}(\lambda_1 \ / \ \lambda_2)$ at $n_e = 10^{12}\text{cm}^{-3}$. (b) n_e dependence of $R^{eff}(\lambda_1 \ / \ \lambda_2)$ at $T_e = 20$ eV. The result by Behrendt is shown for comparison.

FIG. 6. Line intensity ratio R^{eff}(492.2 nm / 471.3 nm) in the presence of hot electrons. (a) $R^{eff}(\lambda_1/\lambda_2)$ at $T_{eh} = 20$ eV and 40 eV, $n_e = 10^{11}$ cm^{-3}. (b) $R^{eff}(\lambda_1/\lambda_2)$ for $T_{eh} = 40$ eV in the high n_e plasmas. The result in the corona model is shown for comparison.

FIG. 7. T_e measurement and investigation of hot electrons in the low n_e experiment. (a) Discharge voltage V_d and electron density n_e. (b) Electron temperatures obtained by the Langmuir probe, T_{ec}(L.P.) and T_{eh}(L.P.), and by the 492.2 nm / 471.3 nm line intensity ratio, T_e(He I) and T_{eh}(He I). The effect of hot electrons is neglected in T_e (He I), while it is included in T_{eh} (He I).

FIG. 8. (a) Experimental result of the line intensities in the low n_e experiment. (b) Line intensity ratio of 492.2 nm / 471.3 nm. The numerical result (Calc.) well reproduces the experimental result by including the effect of hot electrons. (c) Line intensity ratio of 501.6 nm / 492.2 nm. The numerical result using the optical escape factor $\Lambda(n_e \times L)$ (Calc.) is consistent with the experimental one.

FIG. 9. Optical depth of the 53.7 nm photon τ and optical escape factor Λ for He gas temperature of 300 K.

FIG. 10. T_e and n_e measurements in the high n_e experiment. (a) Experimentally observed line intensity ratios. (b) Electron densities obtained from the 492.2 nm / 504.8 nm line intensity ratio, n_e(He I), and by the Langmuir probe, n_e(L.P.). (c) Electron temperatures obtained from the 504.8 nm / 471.3 nm and 492.2 nm / 471.3 nm line intensity ratios, T_e(He I), and T_{eh}(He I), and by the Langmuir probe, T_{ec}(L.P.)

FIG. 11. Effective ionization rate coefficient S^{eff} obtained by the C.R.- model.

FIG. 12. Contribution of the recombining component on the population density of 4^1D, $\mathrm{n(i)}_{recom.}$ / n(i). The ratio of ion to atoms n^+_{He} / n_{He} is 0.1, which is the maximum value in the NAGDIS-I helium discharge.

FIG. A1. Excitation rate coefficient from the ground state C_{1i}. (a) $1^1S - n^1S$, (b) $1^1S - n^1P$, (c) $1^1S - n^1D$, (d) $1^1S - n^3S$, (e) $1^1S - n^3P$, (f) $1^1S - n^3D$.

FIG. A2. Effective emission rate coefficient $C_{em}^{eff}(\lambda)$ for (a) 504.8 nm, (b) 501.6 nm, (c) 492.2 nm, and (d) 471.3 nm.

FIG. A3. (a) T_e- and (b) n_e- dependences of the line radiation power rate coefficient P_{rad}^{eff} defined for the ionizing plasma condition.

FIG. A4. (a) T_e- and (b) n_e- dependences of the normalized population densities $n(i)/n_{He}$ for the 2^1S and 2^3S metastable states.

FIG. B1. Ratio of effective rate coefficients for ionization to emission, $S^{eff}/C_{em}^{eff}(\lambda)$, for (a) 504.8 nm, (b) 501.6 nm, (c) 492.2 nm, and (d) 471.3 nm.

FIG. B2. The n_e dependence of $R^{eff}(\lambda_1/\lambda_2)$ summarized for experimental use. (a) R^{eff}(492.2 nm / 504.8 nm) for n_e measurement. (b) R^{eff}(504.8 nm / 471.3 nm) for T_e measurement. (c) R^{eff}(492.2 nm / 471.3 nm) for T_e measurement.

FIG. B3. The T_e dependence of R^{eff}(504.8 nm / 471.3 nm) for T_e measurement (a) n_e = 10^{11} - 10^{12} cm^{-3}. (b) n_e = 10^{12} - 10^{13} cm^{-3}. (c) n_e = 10^{13} - 10^{14} cm^{-3}.

FIG. B4. The T_e dependence of R^{eff}(492.2 nm / 471.3 nm) for T_e measurement (a) n_e = 10^{11} - 10^{12} cm^{-3}. (b) n_e = 10^{12} - 10^{13} cm^{-3}. (c) n_e = 10^{13} - 10^{14} cm^{-3}.

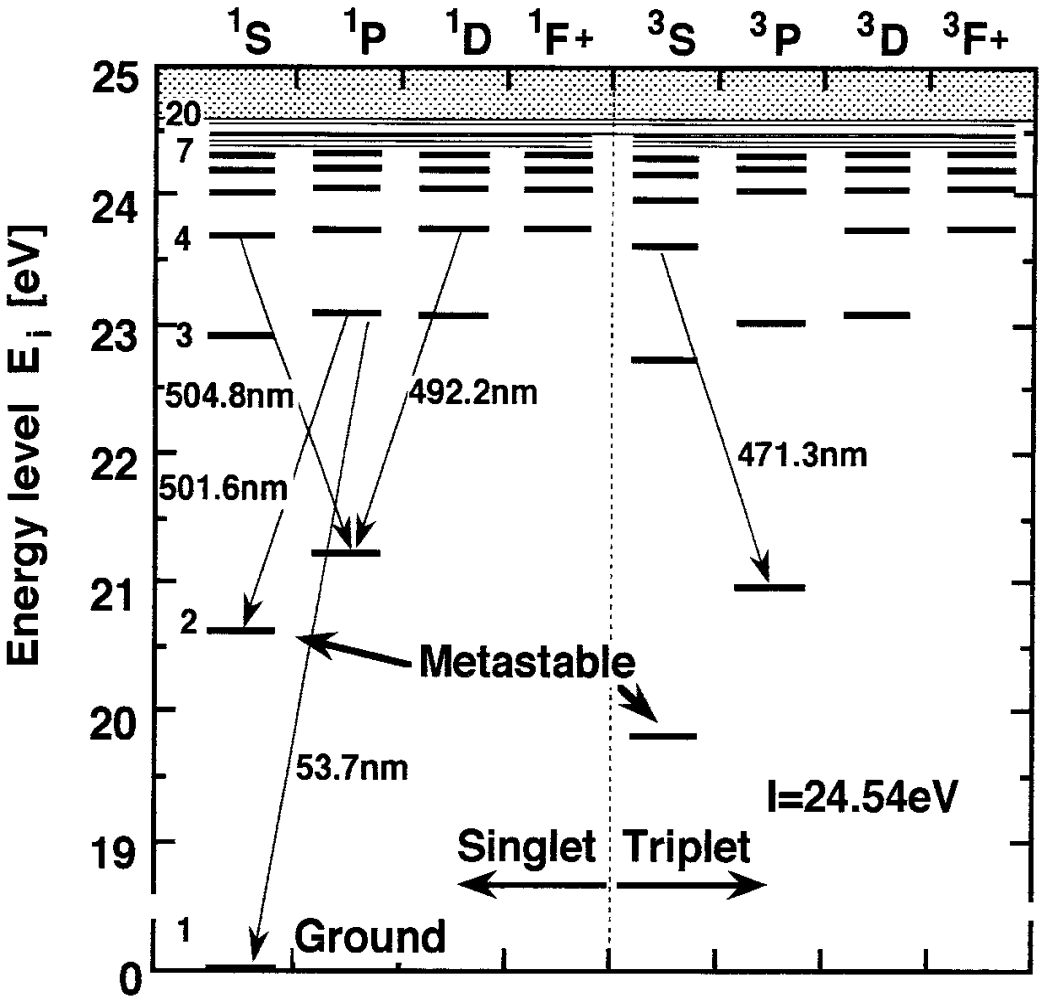
^1S ^1P ^1D $^1F+$ ^3S ^3P ^3D $^3F+$
Energy level E_i [eV]
25
24
23
22
21
20
19
0
20
7
4
3
2
1
504.8nm
501.6nm
492.2nm
471.3nm
53.7nm
Metastable
Ground
Singlet
Triplet
I=24.54eV

Fig. 1

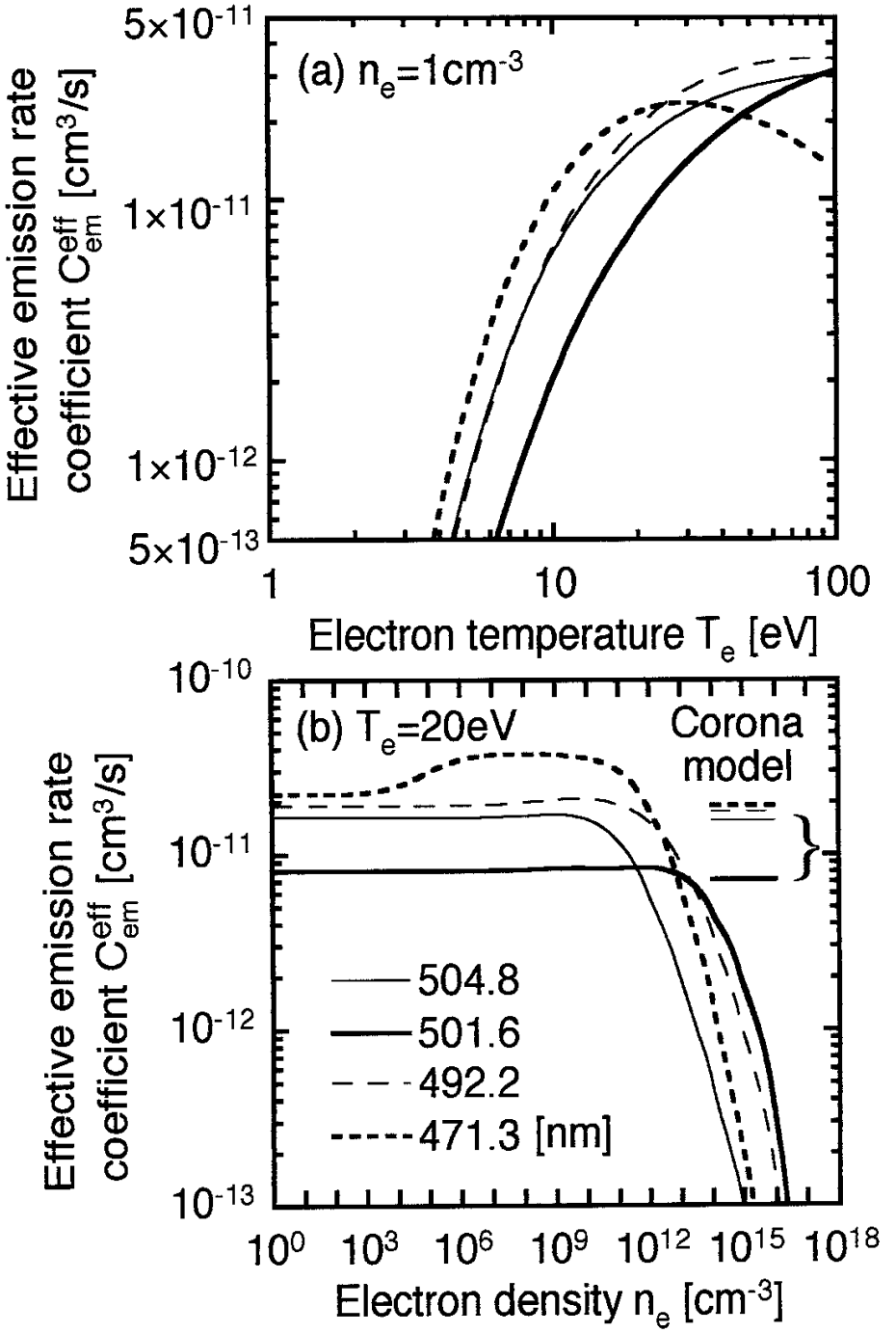
(a) n_e=1cm^{-3}
Effective emission rate coefficient C_{em}^{eff} [cm^3/s]
5×10^{-11}
1×10^{-11}
1×10^{-12}
5×10^{-13}
1
10
100
Electron temperature T_e [eV]
(b) T_e=20eV
Corona model
504.8
501.6
492.2
471.3 [nm]
10^{-10}
10^{-11}
10^{-12}
10^{-13}
10^0 10^3 10^6 10^9 10^{12} 10^{15} 10^{18}
Electron density n_e [cm^{-3}]

Fig. 2

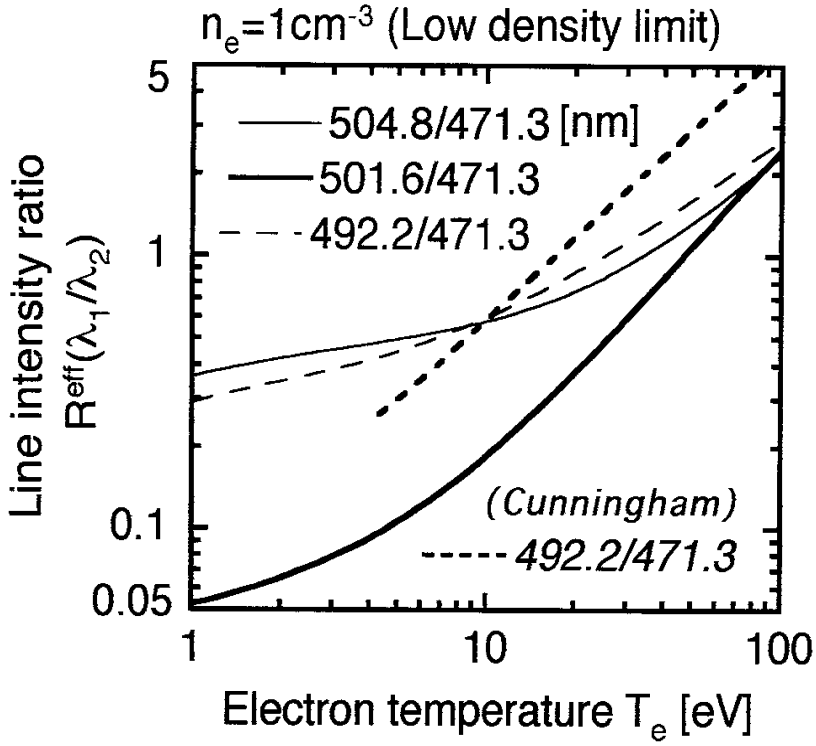
n_e=1cm^{-3} (Low density limit)
5
1
0.1
0.05
Line intensity ratio
$R^{eff}(\lambda_1/\lambda_2)$
504.8/471.3 [nm]
501.6/471.3
492.2/471.3
(Cunningham)
492.2/471.3
1
10
100
Electron temperature T_e [eV]

Fig. 3

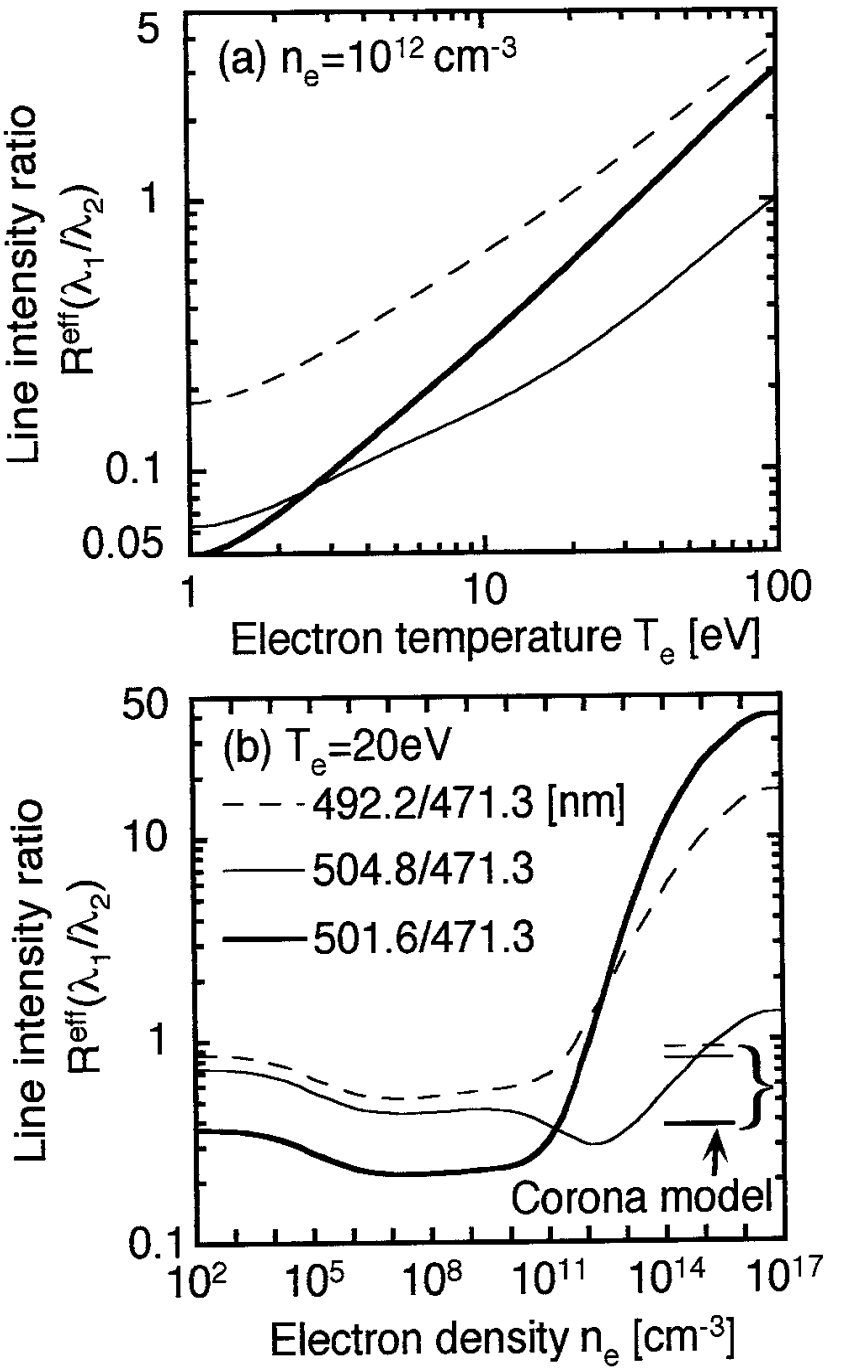
(a) $n_e=10^{12}$ cm^{-3}
Line intensity ratio
$R^{eff}(\lambda_1/\lambda_2)$
5
1
0.1
0.05
1
10
100
Electron temperature T_e [eV]
(b) T_e=20eV
492.2/471.3 [nm]
504.8/471.3
501.6/471.3
Corona model
50
10
1
0.1
10^2
10^5
10^8
10^{11}
10^{14}
10^{17}
Electron density n_e [cm^{-3}]

Fig.4

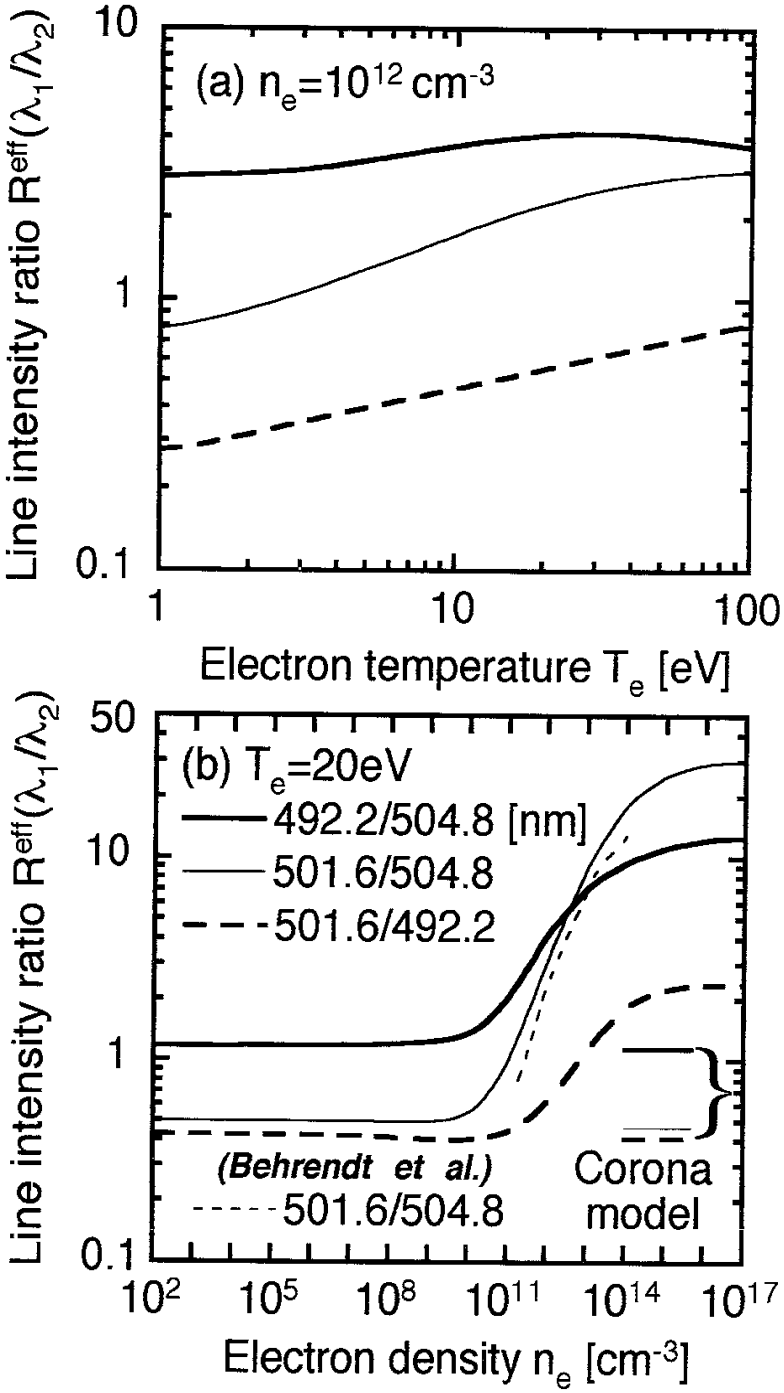
(a) $n_e=10^{12}$ cm^{-3}
Line intensity ratio $R^{eff}(\lambda_1/\lambda_2)$
10
1
0.1
1
10
100
Electron temperature T_e [eV]
(b) T_e=20eV
492.2/504.8 [nm]
501.6/504.8
501.6/492.2
(Behrendt et al.)
501.6/504.8
Corona model
50
10
1
0.1
10^2
10^5
10^8
10^{11}
10^{14}
10^{17}
Electron density n_e [cm^{-3}]

Fig. 5

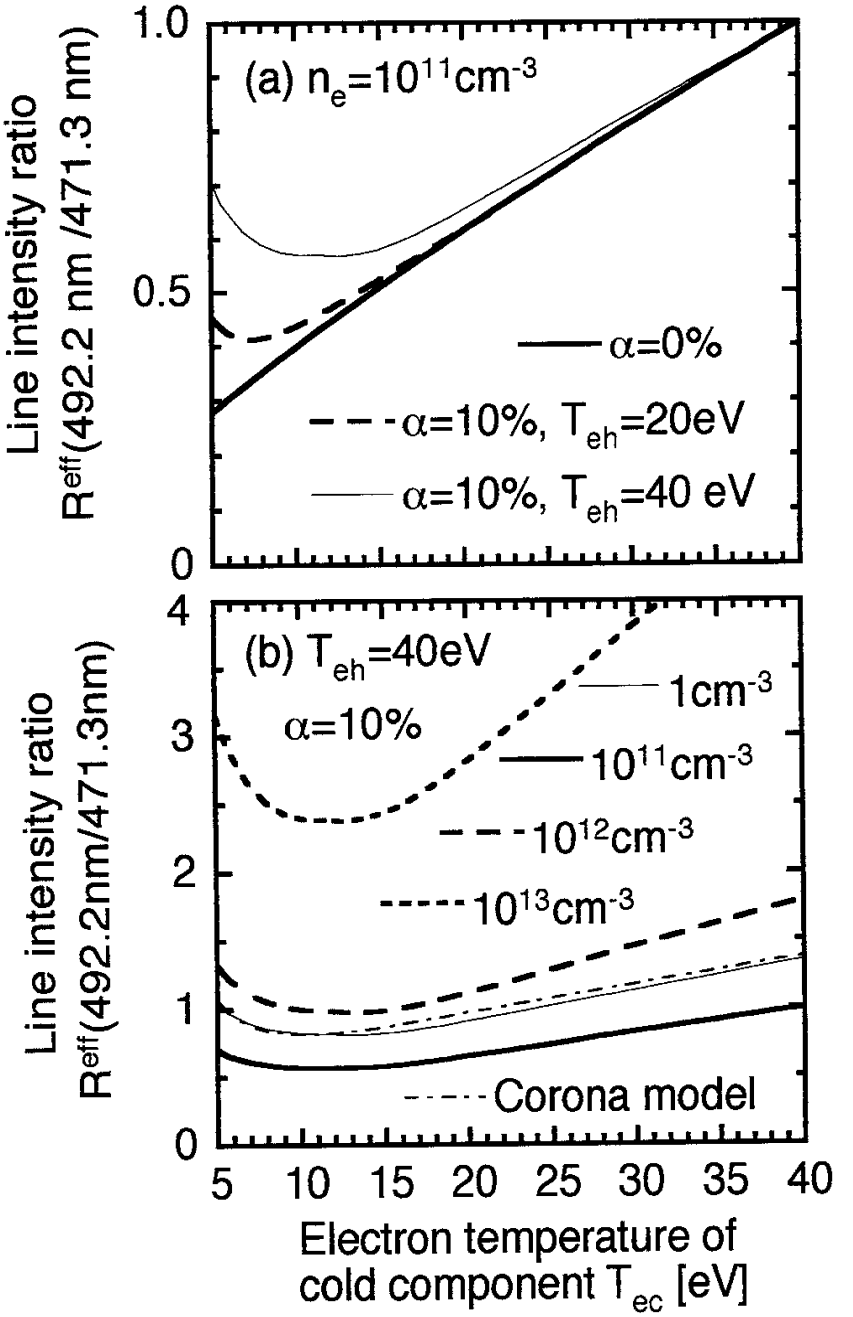
1.0
0.5
0
(a) $n_e=10^{11}cm^{-3}$
Line intensity ratio
R^{eff}(492.2 nm /471.3 nm)
α=0%
α=10%, T_{eh}=20eV
α=10%, T_{eh}=40 eV
4
3
2
1
0
(b) T_{eh}=40eV
α=10%
1cm^{-3}
$10^{11}cm^{-3}$
$10^{12}cm^{-3}$
$10^{13}cm^{-3}$
Corona model
Line intensity ratio
R^{eff}(492.2nm/471.3nm)
5 10 15 20 25 30 35 40
Electron temperature of
cold component T_{ec} [eV]

Fig. 6

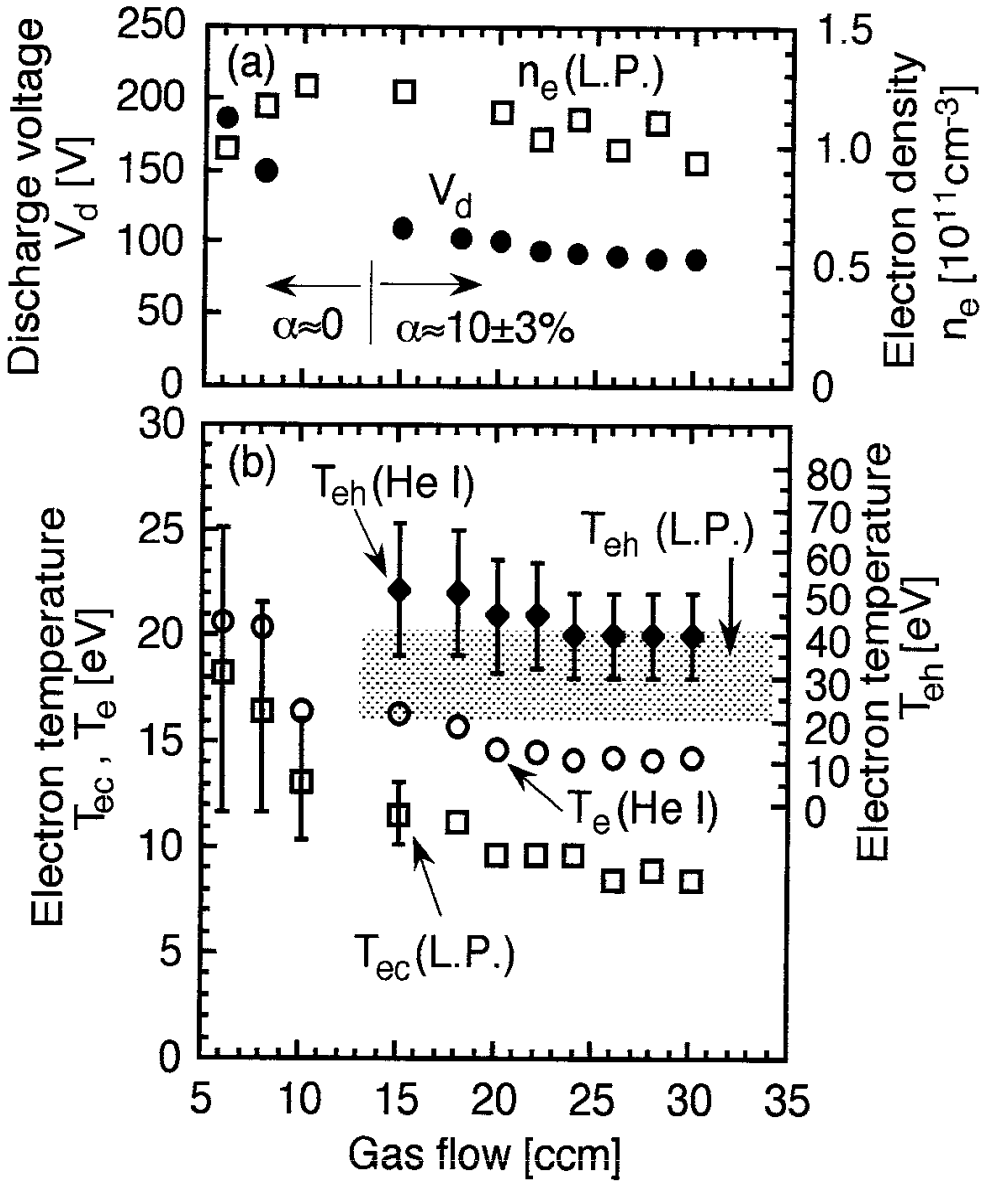
(a)
n_e(L.P.)
V_d
α≈0
α≈10±3%
Discharge voltage V_d [V]
Electron density n_e [10^{11}cm^{-3}]
250
200
150
100
50
0
1.5
1.0
0.5
0
(b)
T_{eh}(He I)
T_{eh} (L.P.)
T_e(He I)
T_{ec}(L.P.)
Electron temperature T_{ec} , T_e [eV]
Electron temperature T_{eh} [eV]
30
25
20
15
10
5
0
80
70
60
50
40
30
20
10
0
5
10
15
20
25
30
35
Gas flow [ccm]

Fig. 7

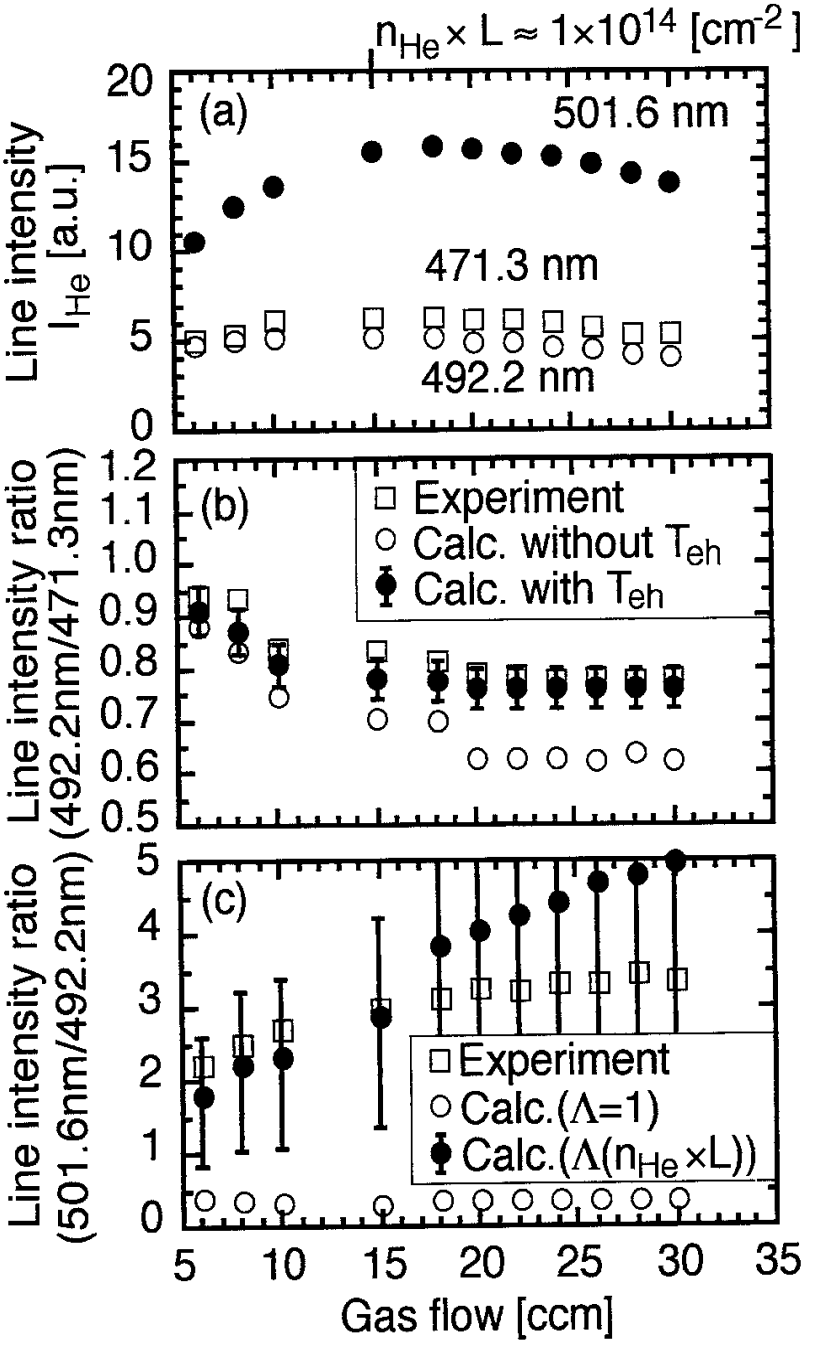
$n_{He} \times L \approx 1 \times 10^{14}$ [cm^{-2}]
(a)
501.6 nm
471.3 nm
492.2 nm
Line intensity I_{He} [a.u.]
(b)
Experiment
Calc. without T_{eh}
Calc. with T_{eh}
Line intensity ratio (492.2nm/471.3nm)
(c)
Experiment
Calc.(Λ=1)
Calc.(Λ(n_{He}×L))
Line intensity ratio (501.6nm/492.2nm)
Gas flow [ccm]

Fig. 8

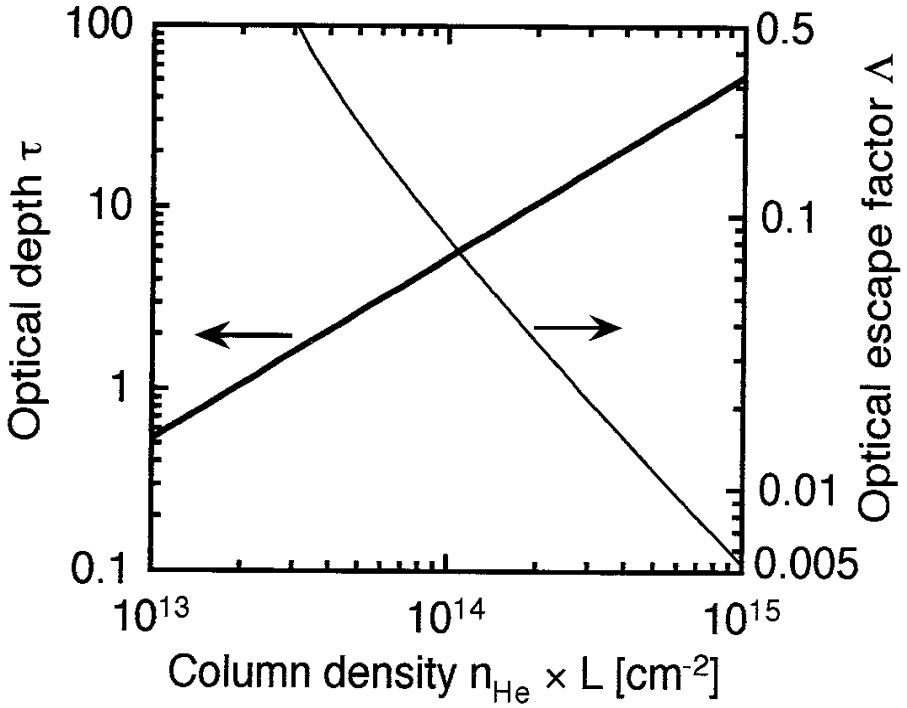
100
10
1
0.1
Optical depth τ
0.5
0.1
0.01
0.005
Optical escape factor Λ
10^13
10^14
10^15
Column density n_He × L [cm^-2]

Fig. 9

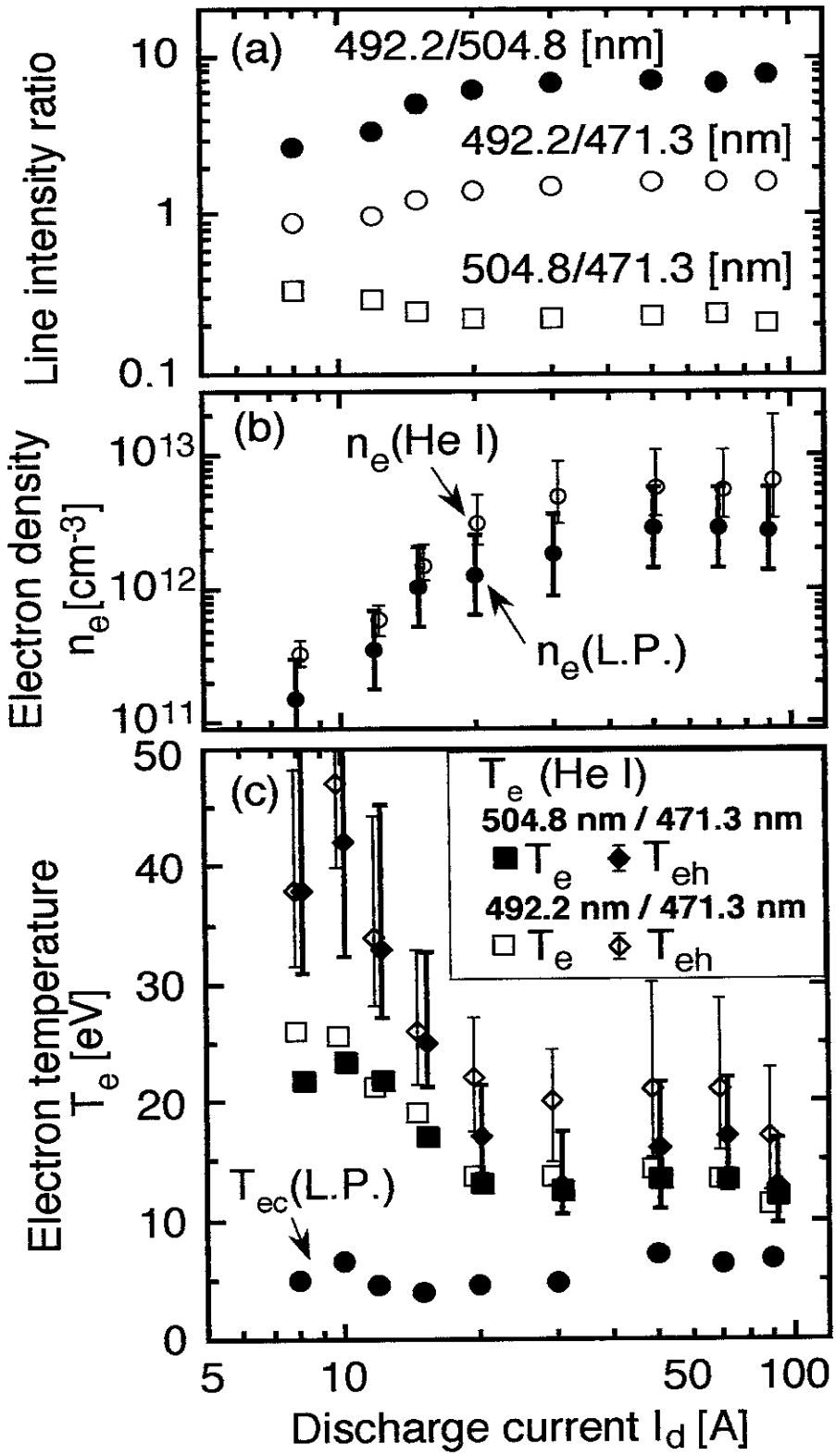
(a)
492.2/504.8 [nm]
492.2/471.3 [nm]
504.8/471.3 [nm]
Line intensity ratio
10
1
0.1
(b)
n_e(He I)
n_e(L.P.)
Electron density
n_e[cm^{-3}]
10^{13}
10^{12}
10^{11}
(c)
T_e (He I)
504.8 nm / 471.3 nm
T_e T_{eh}
492.2 nm / 471.3 nm
T_e T_{eh}
T_{ec}(L.P.)
Electron temperature
T_e [eV]
50
40
30
20
10
0
5
10
50
100
Discharge current I_d [A]

Fig.10

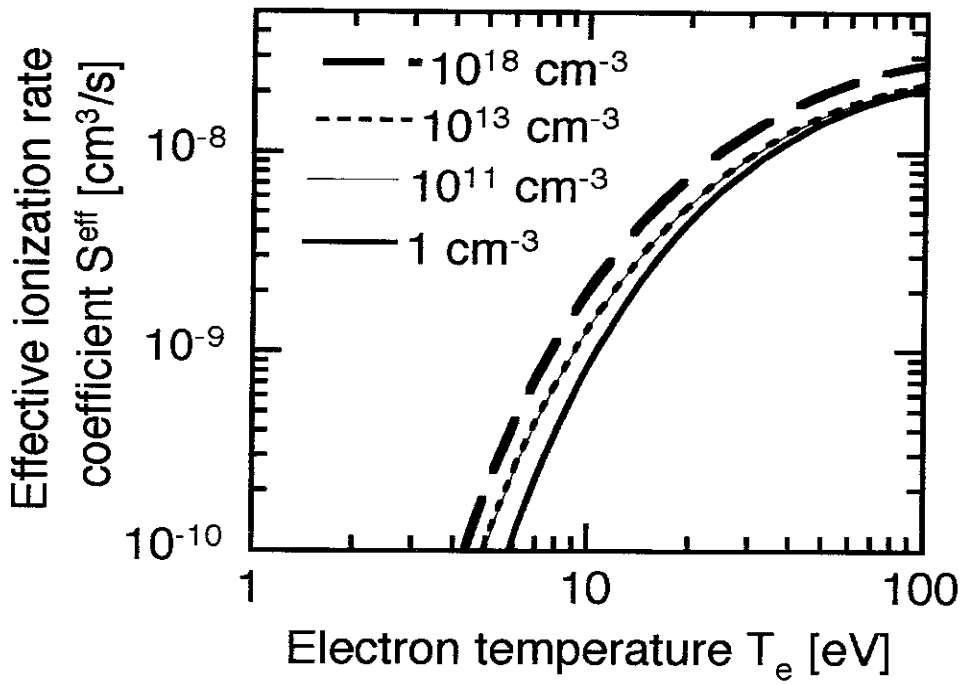
Effective ionization rate coefficient S^{eff} [cm^3/s]
10^{18} cm^{-3}
10^{13} cm^{-3}
10^{11} cm^{-3}
1 cm^{-3}
10^{-8}
10^{-9}
10^{-10}
1
10
100
Electron temperature T_e [eV]

Fig. 11

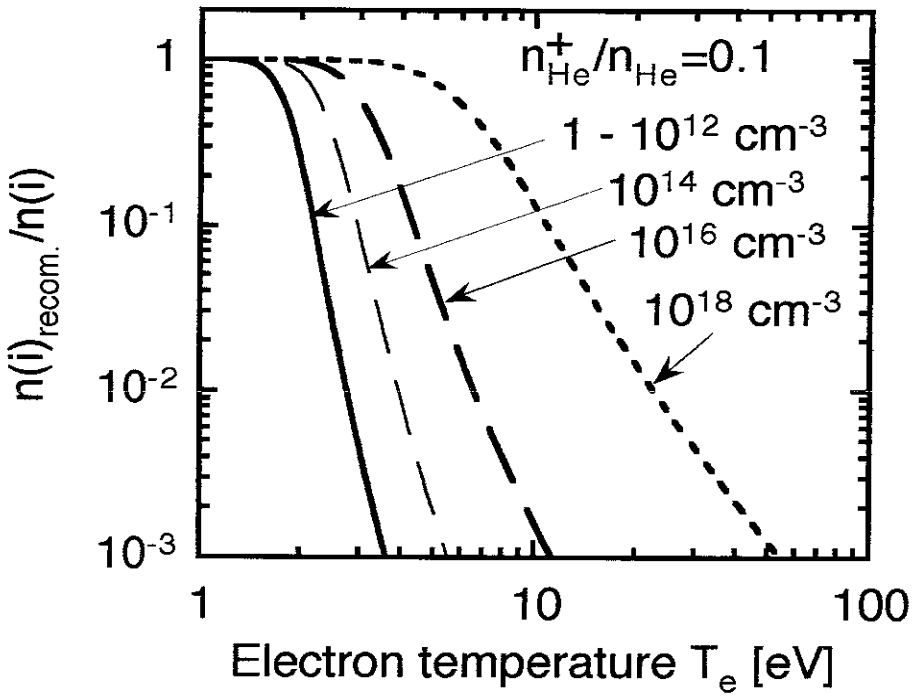
$n(i)_{recom.}/n(i)$
n^+_{He}/n_{He}=0.1
1 - 10^{12} cm^{-3}
10^{14} cm^{-3}
10^{16} cm^{-3}
10^{18} cm^{-3}
1
10^{-1}
10^{-2}
10^{-3}
1
10
100
Electron temperature T_e [eV]

Fig. 12

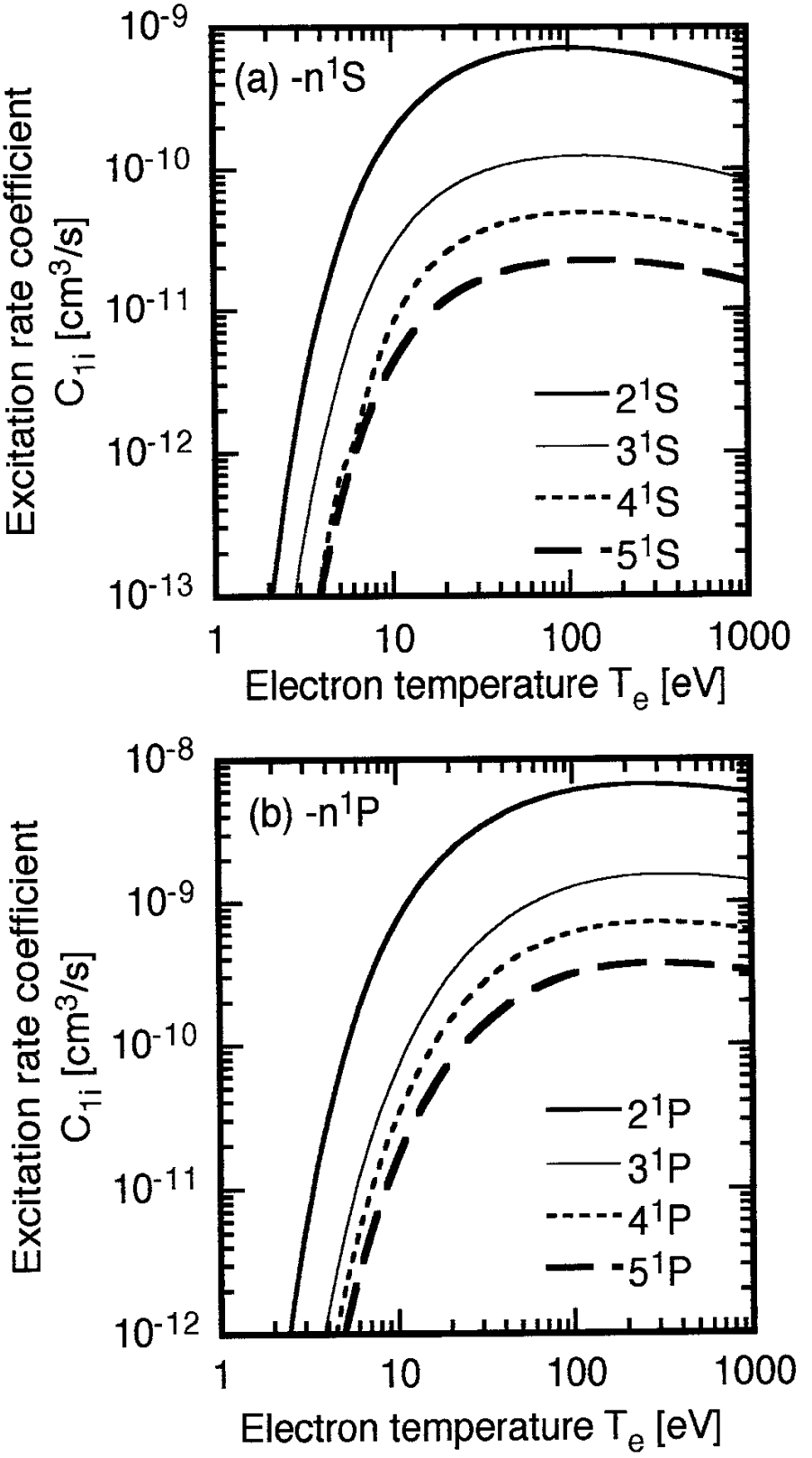
(a) -n1S
Excitation rate coefficient
C1i [cm3/s]
10-9
10-10
10-11
10-12
10-13
21S
31S
41S
51S
1
10
100
1000
Electron temperature Te [eV]
(b) -n1P
Excitation rate coefficient
C1i [cm3/s]
10-8
10-9
10-10
10-11
10-12
21P
31P
41P
51P
1
10
100
1000
Electron temperature Te [eV]

Fig. A1

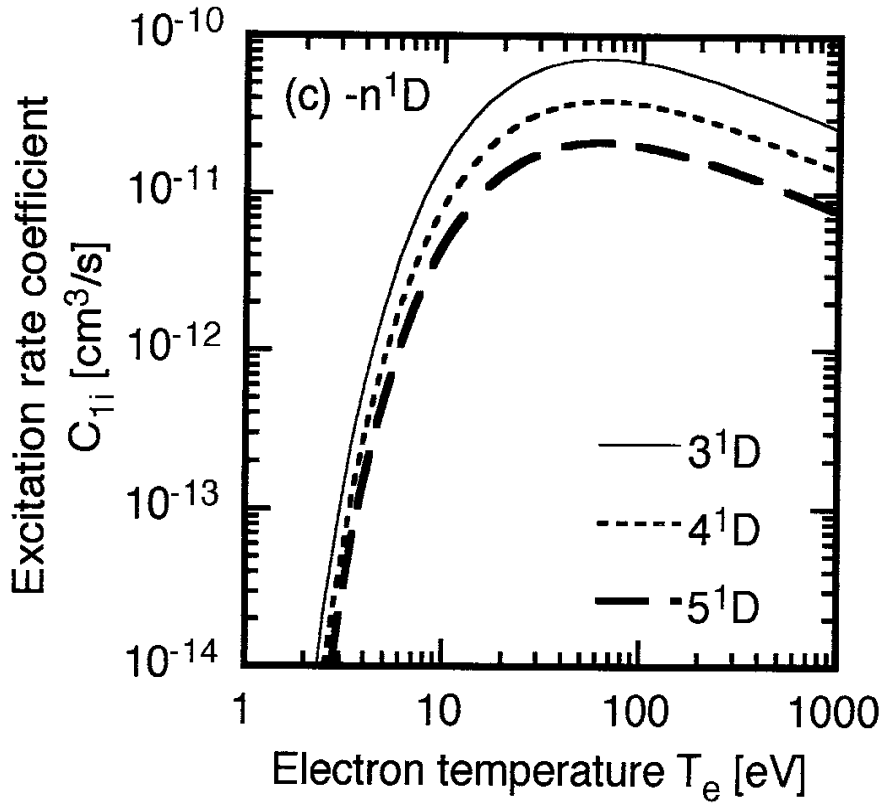
(c) -n¹D
Excitation rate coefficient
C1i [cm³/s]
10-10
10-11
10-12
10-13
10-14
3¹D
4¹D
5¹D
1
10
100
1000
Electron temperature Te [eV]

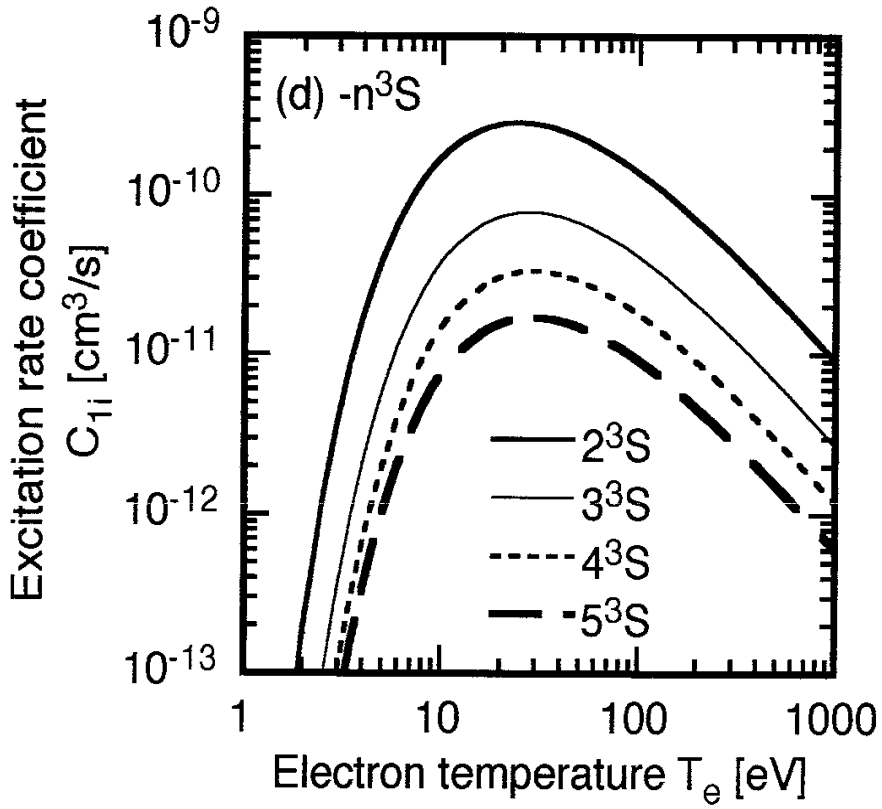
(d) -n³S
Excitation rate coefficient
C1i [cm³/s]
10-9
10-10
10-11
10-12
10-13
2³S
3³S
4³S
5³S
1
10
100
1000
Electron temperature Te [eV]

Fig. A1

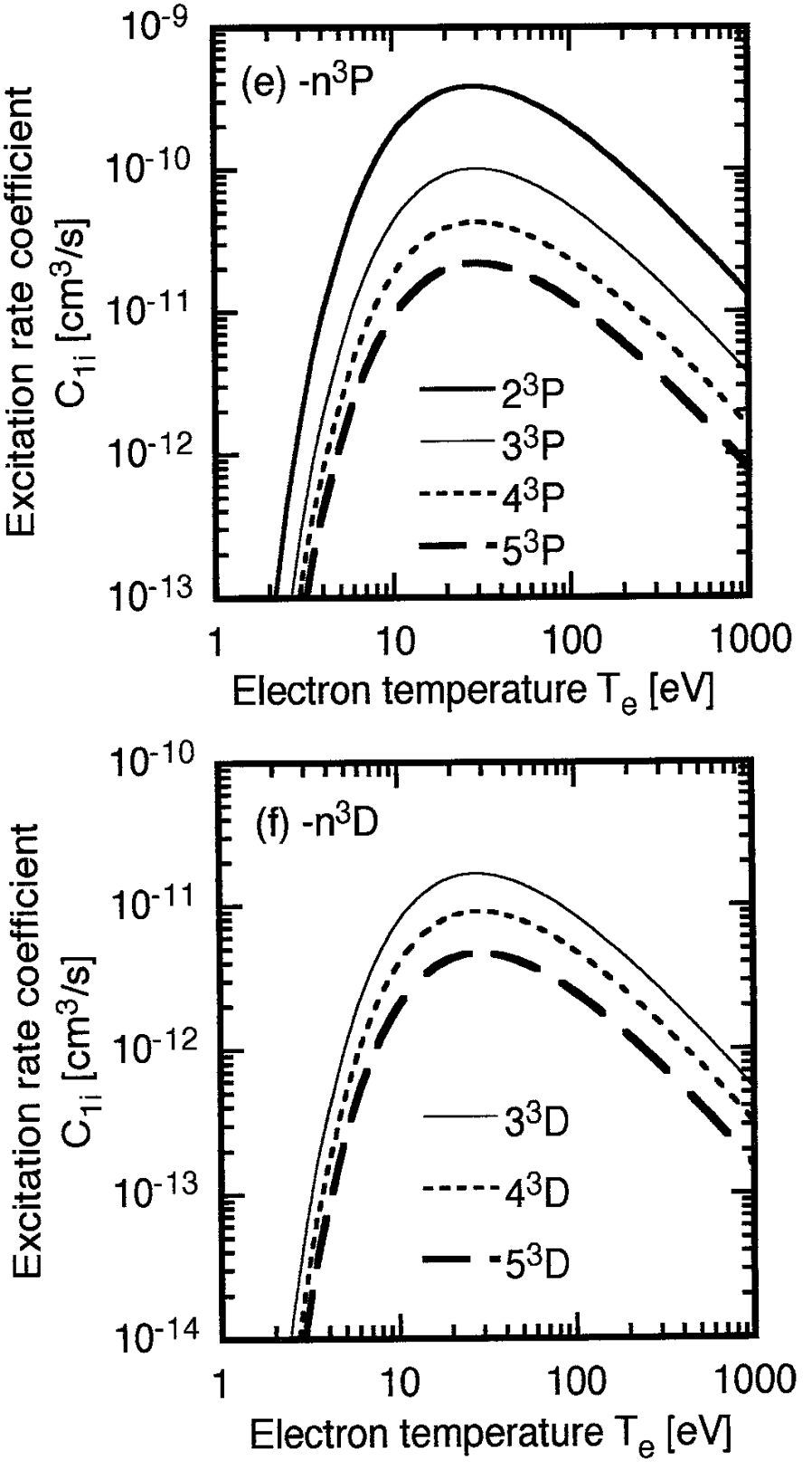
(e) -n3P
Excitation rate coefficient
C1i [cm3/s]
10-9
10-10
10-11
10-12
10-13
2 3P
3 3P
4 3P
5 3P
1
10
100
1000
Electron temperature Te [eV]
(f) -n3D
Excitation rate coefficient
C1i [cm3/s]
10-10
10-11
10-12
10-13
10-14
3 3D
4 3D
5 3D
1
10
100
1000
Electron temperature Te [eV]

Fig. A1

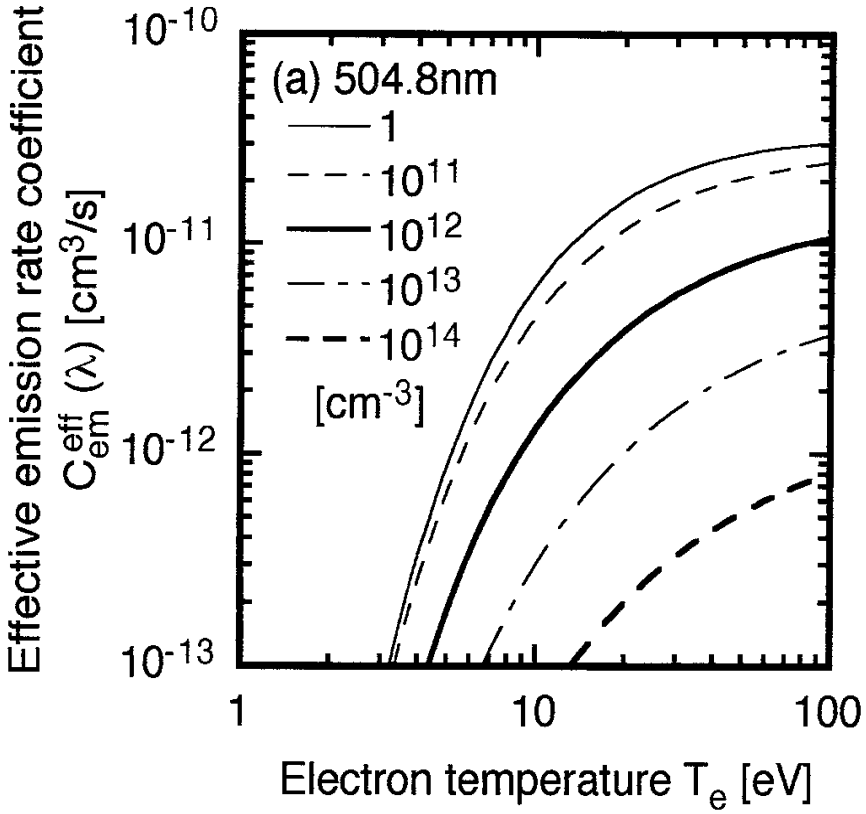
(a) 504.8nm
1
10^11
10^12
10^13
10^14
[cm^-3]
Effective emission rate coefficient
C_em^eff (λ) [cm^3/s]
10^-10
10^-11
10^-12
10^-13
1
10
100
Electron temperature T_e [eV]

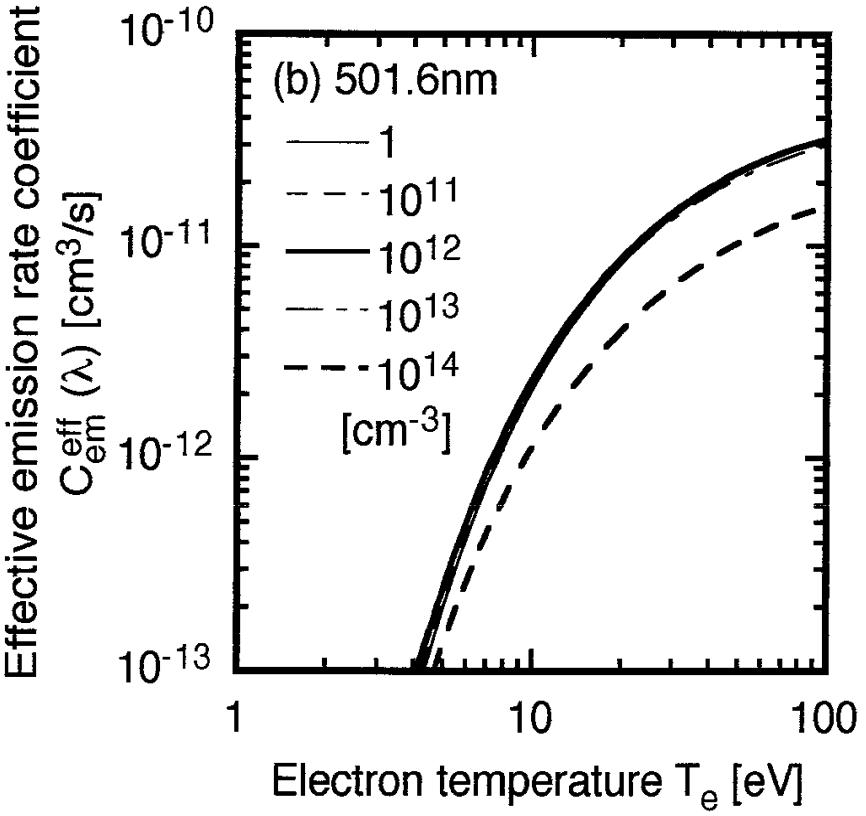
(b) 501.6nm
1
10^11
10^12
10^13
10^14
[cm^-3]
Effective emission rate coefficient
C_em^eff (λ) [cm^3/s]
10^-10
10^-11
10^-12
10^-13
1
10
100
Electron temperature T_e [eV]

Fig. A2

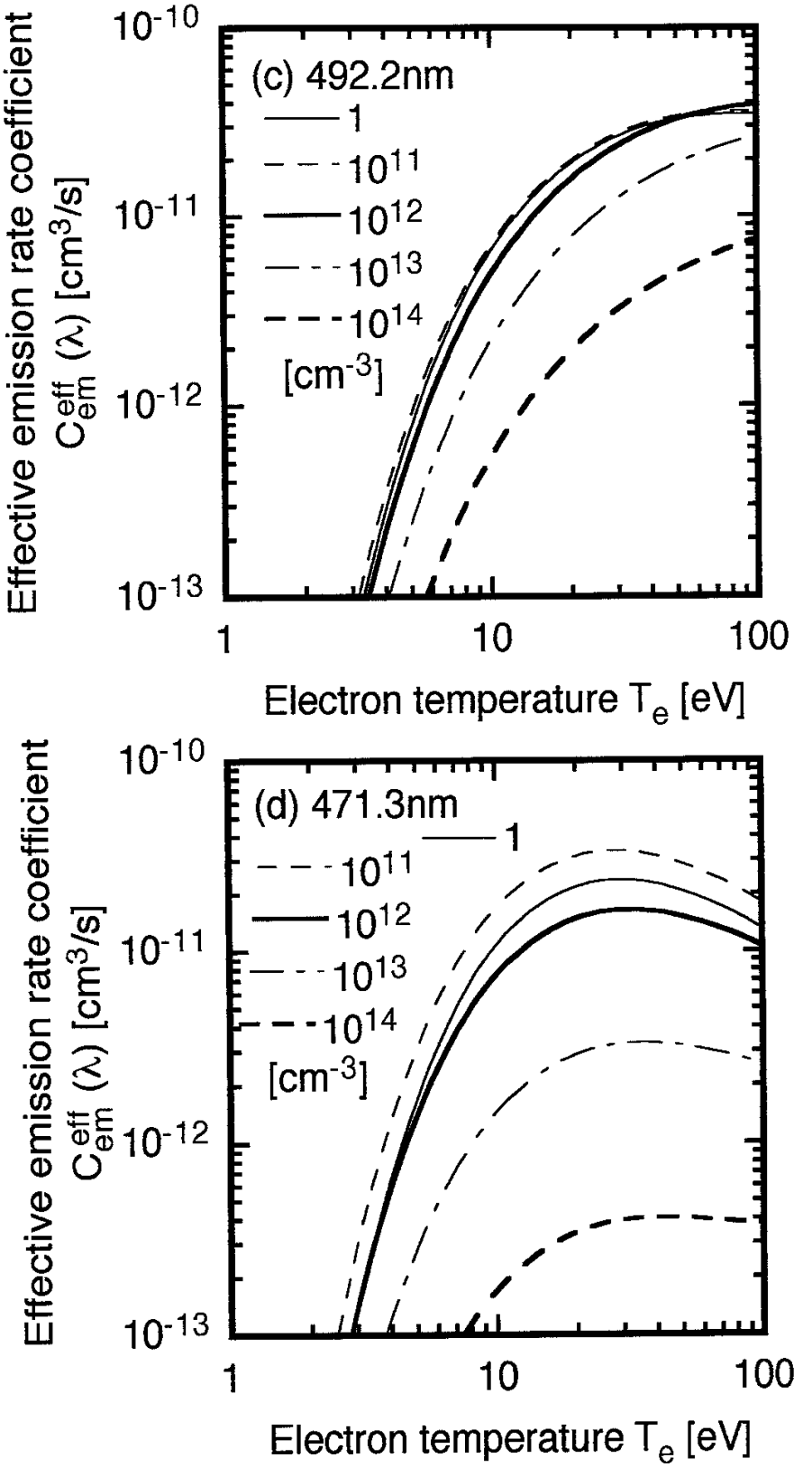
(c) 492.2nm
1
10^11
10^12
10^13
10^14
[cm^-3]
Effective emission rate coefficient
C_em^eff (λ) [cm^3/s]
10^-10
10^-11
10^-12
10^-13
1
10
100
Electron temperature T_e [eV]
(d) 471.3nm
1
10^11
10^12
10^13
10^14
[cm^-3]
Effective emission rate coefficient
C_em^eff (λ) [cm^3/s]
10^-10
10^-11
10^-12
10^-13
1
10
100
Electron temperature T_e [eV]

Fig. A2

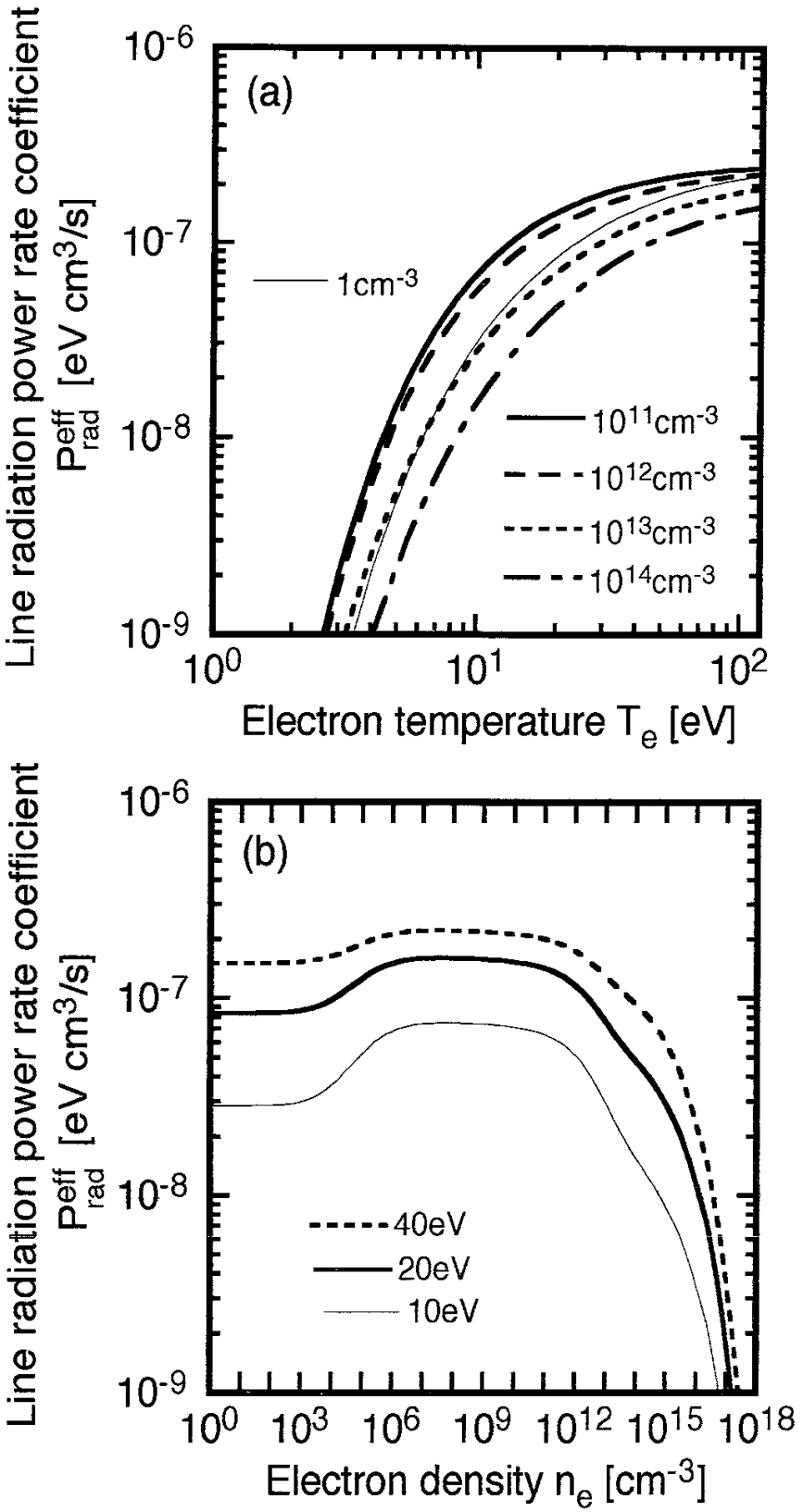
(a)
Line radiation power rate coefficient
P^{eff}_{rad} [eV cm^3/s]
10^{-6}
10^{-7}
10^{-8}
10^{-9}
1cm^{-3}
10^{11}cm^{-3}
10^{12}cm^{-3}
10^{13}cm^{-3}
10^{14}cm^{-3}
10^0
10^1
10^2
Electron temperature T_e [eV]
(b)
Line radiation power rate coefficient
P^{eff}_{rad} [eV cm^3/s]
10^{-6}
10^{-7}
10^{-8}
10^{-9}
40eV
20eV
10eV
10^0 10^3 10^6 10^9 10^{12} 10^{15} 10^{18}
Electron density n_e [cm^{-3}]

Fig. A3

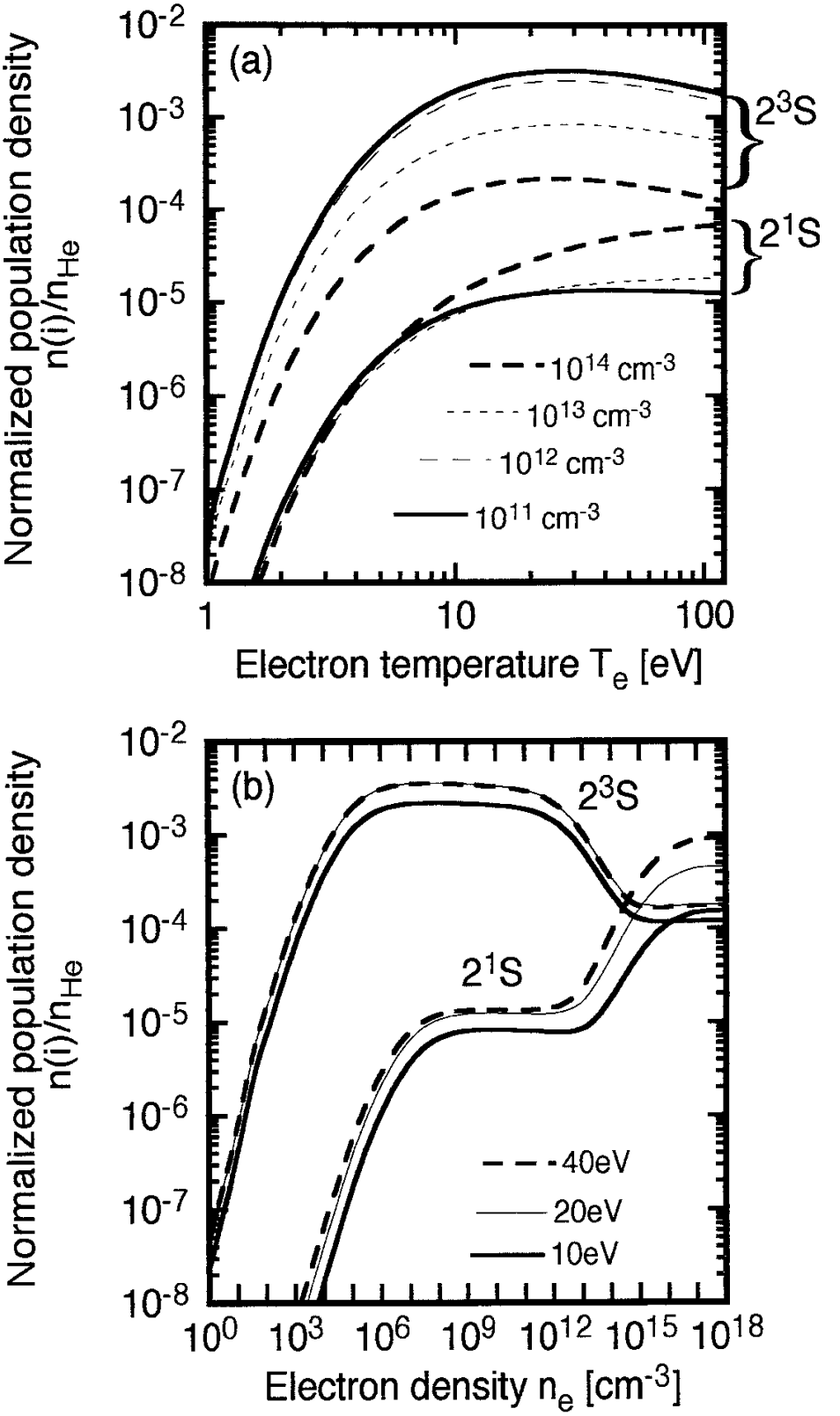
(a)
Normalized population density
n(i)/n_He
10^-2
10^-3
10^-4
10^-5
10^-6
10^-7
10^-8
1
10
100
Electron temperature T_e [eV]
2^3S
2^1S
10^14 cm^-3
10^13 cm^-3
10^12 cm^-3
10^11 cm^-3
(b)
2^3S
2^1S
40eV
20eV
10eV
10^0
10^3
10^6
10^9
10^12
10^15
10^18
Electron density n_e [cm^-3]

Fig. A4

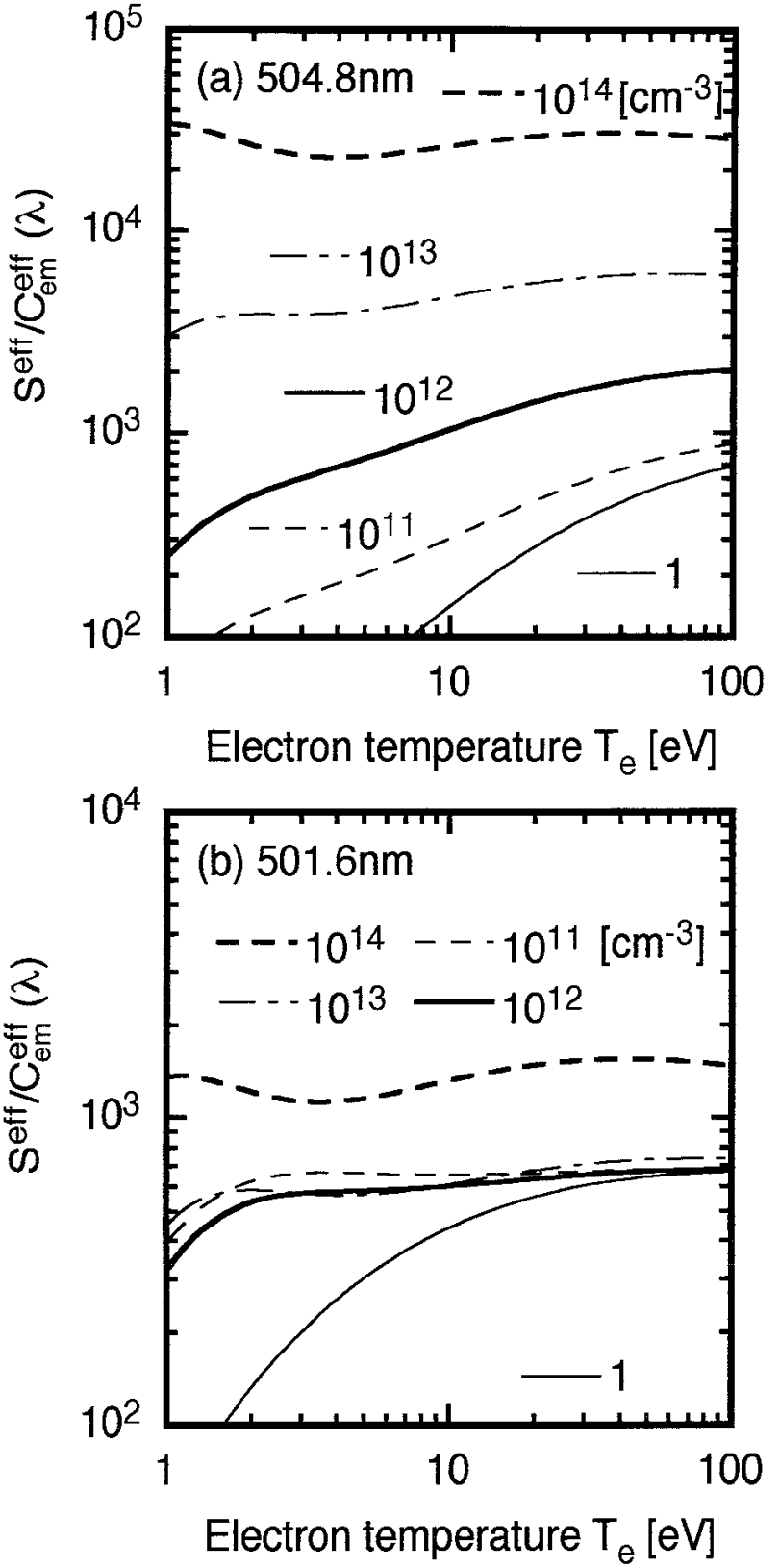
(a) 504.8nm
10^14 [cm^-3]
10^13
10^12
10^11
1
10^5
10^4
10^3
10^2
S^eff/C^eff_em (λ)
1
10
100
Electron temperature T_e [eV]
(b) 501.6nm
10^14
10^11 [cm^-3]
10^13
10^12
1
10^4
10^3
10^2
S^eff/C^eff_em (λ)
1
10
100
Electron temperature T_e [eV]

Fig. B1

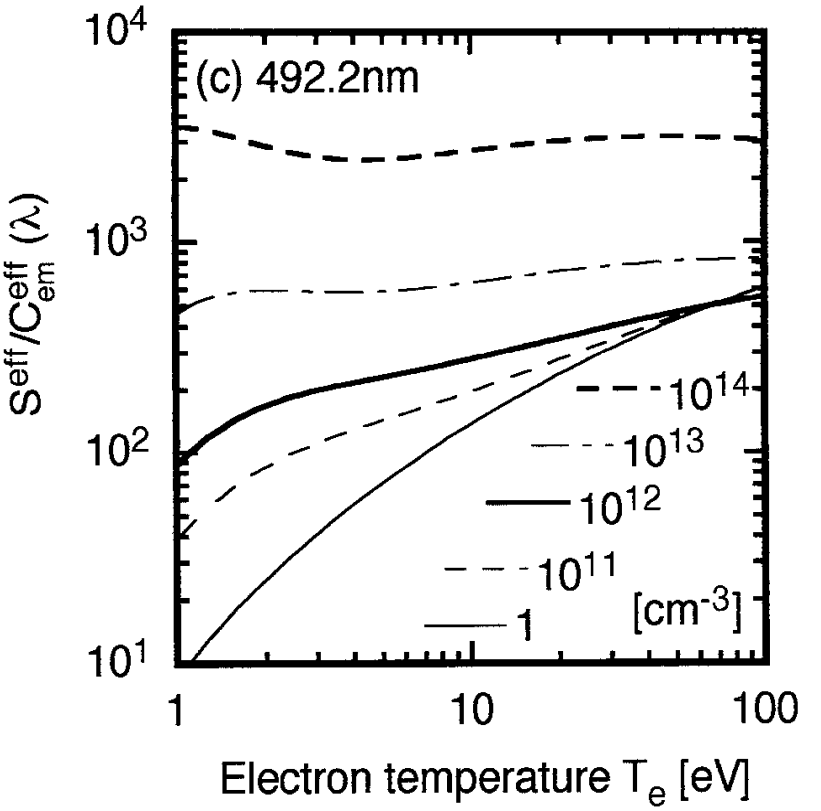
(c) 492.2nm
10^4
10^3
10^2
10^1
S^{eff}/C^{eff}_{em} (λ)
10^{14}
10^{13}
10^{12}
10^{11}
1
[cm^{-3}]
1
10
100
Electron temperature T_e [eV]

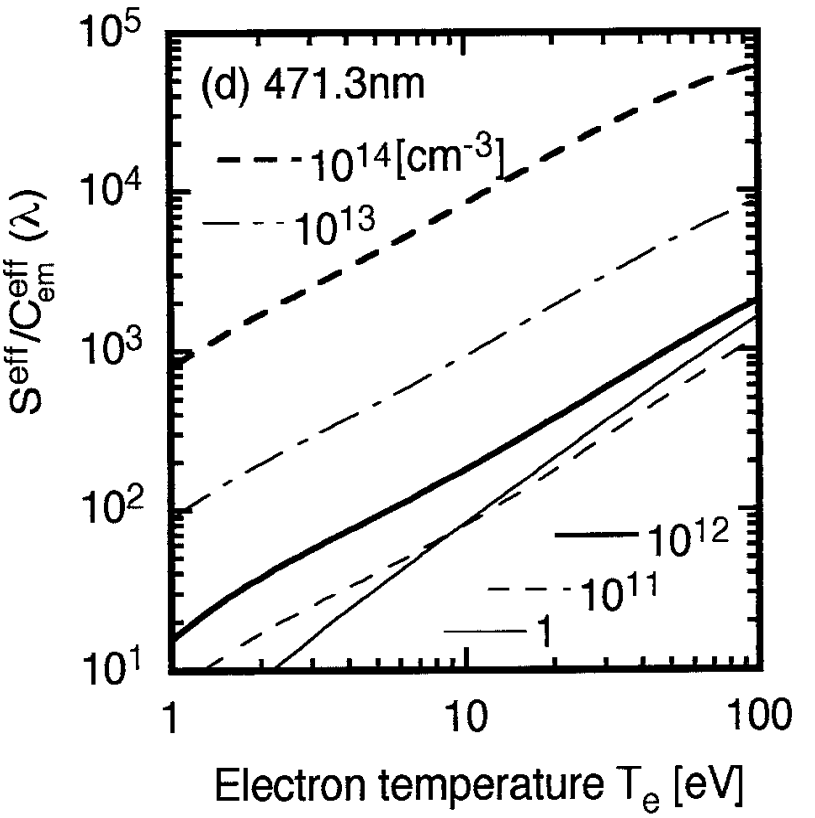
(d) 471.3nm
10^5
10^4
10^3
10^2
10^1
S^{eff}/C^{eff}_{em} (λ)
10^{14}[cm^{-3}]
10^{13}
10^{12}
10^{11}
1
1
10
100
Electron temperature T_e [eV]

Fig. B1

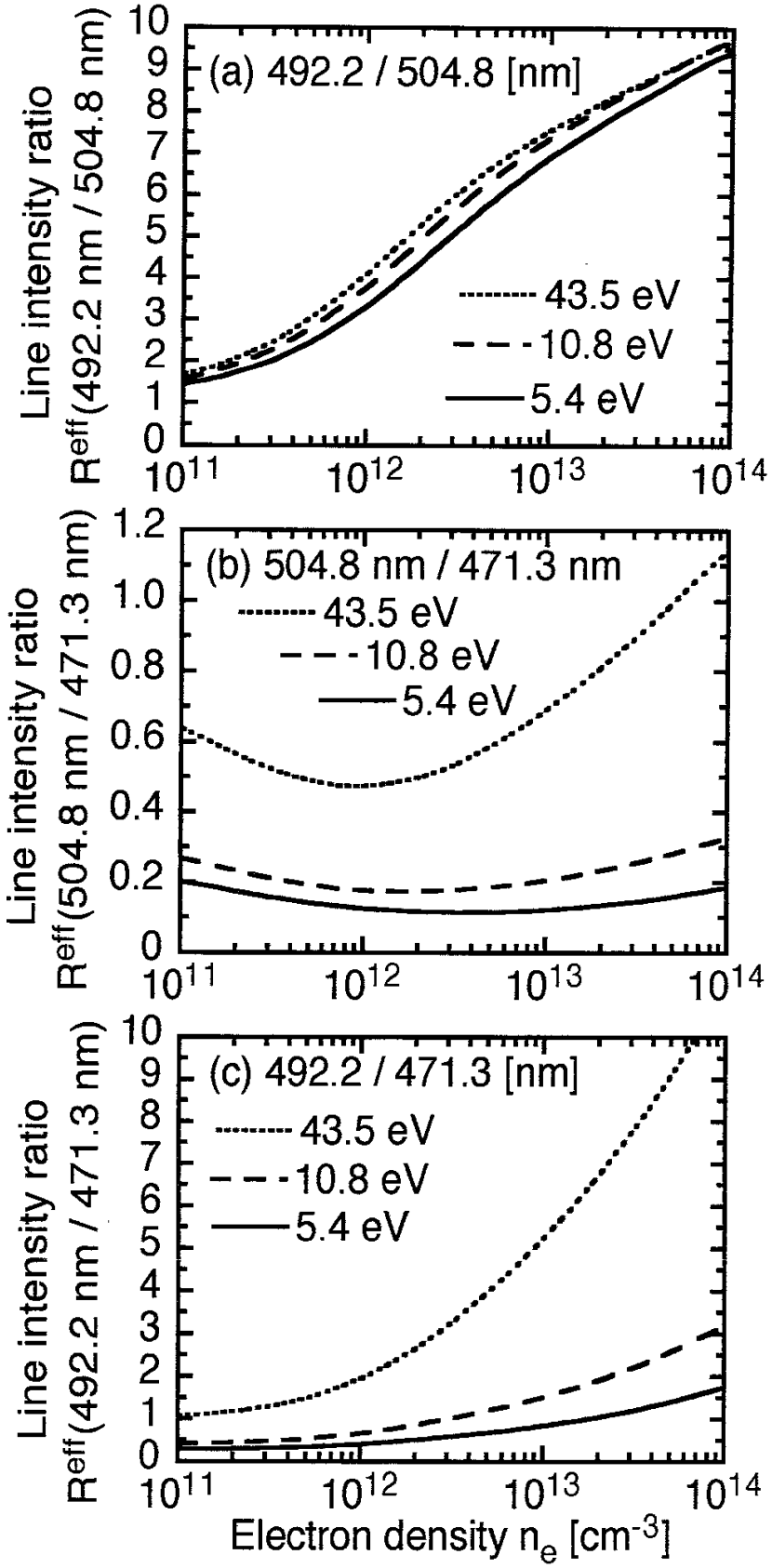
(a) 492.2 / 504.8 [nm]
43.5 eV
10.8 eV
5.4 eV
Line intensity ratio
R^{eff}(492.2 nm / 504.8 nm)
(b) 504.8 nm / 471.3 nm
43.5 eV
10.8 eV
5.4 eV
Line intensity ratio
R^{eff}(504.8 nm / 471.3 nm)
(c) 492.2 / 471.3 [nm]
43.5 eV
10.8 eV
5.4 eV
Line intensity ratio
R^{eff}(492.2 nm / 471.3 nm)
10^{11}
10^{12}
10^{13}
10^{14}
Electron density n_e [cm^{-3}]

Fig. B2

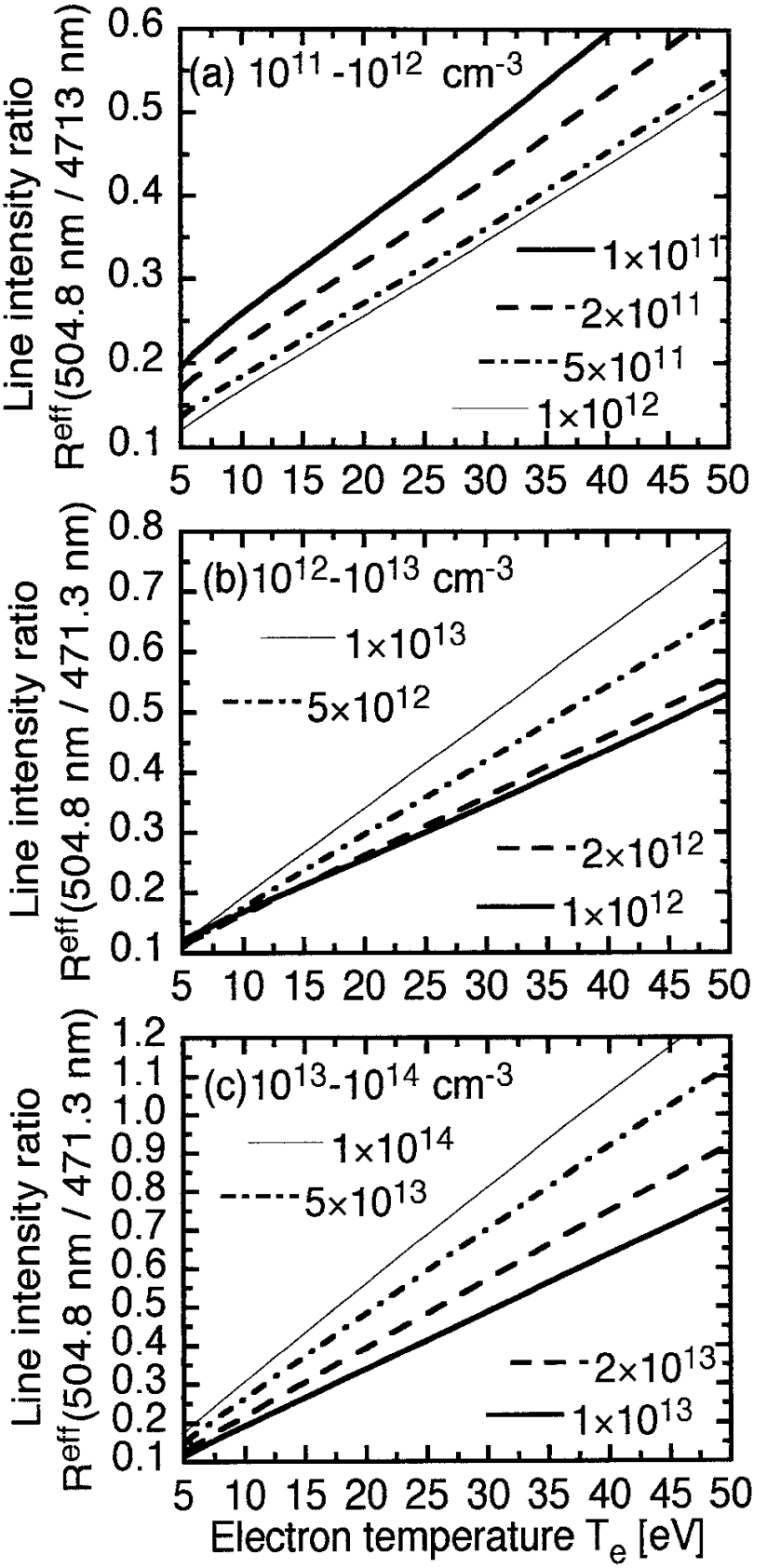
Line intensity ratio
R^{eff}(504.8 nm / 4713 nm)
(a) 10^{11}-10^{12} cm^{-3}
1×10^{11}
2×10^{11}
5×10^{11}
1×10^{12}
Line intensity ratio
R^{eff}(504.8 nm / 471.3 nm)
(b)10^{12}-10^{13} cm^{-3}
1×10^{13}
5×10^{12}
2×10^{12}
1×10^{12}
Line intensity ratio
R^{eff}(504.8 nm / 471.3 nm)
(c)10^{13}-10^{14} cm^{-3}
1×10^{14}
5×10^{13}
2×10^{13}
1×10^{13}
Electron temperature T_e [eV]

Fig. B3

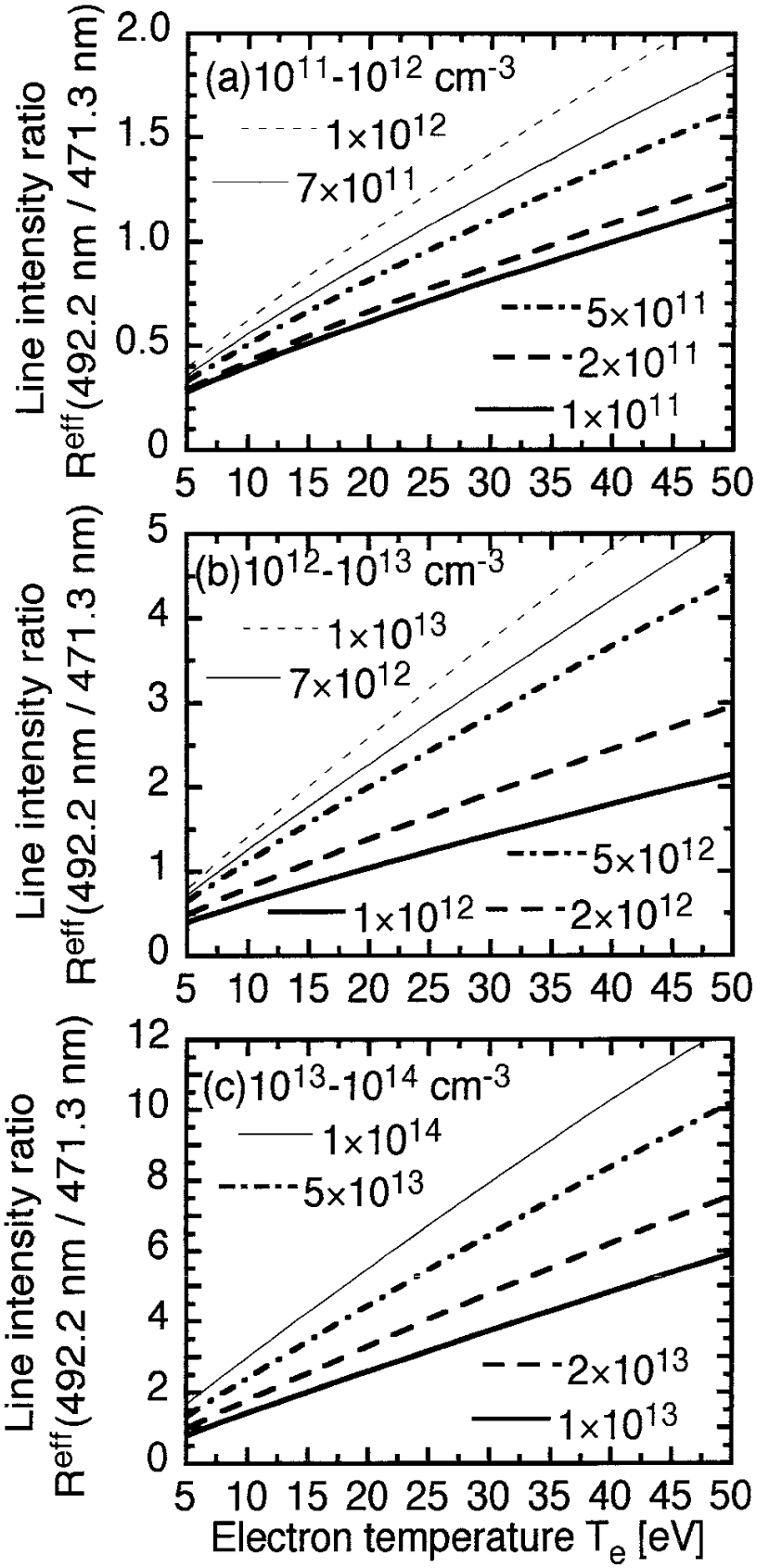
(a)10^11-10^12 cm^-3
1×10^12
7×10^11
5×10^11
2×10^11
1×10^11
(b)10^12-10^13 cm^-3
1×10^13
7×10^12
5×10^12
1×10^12
2×10^12
(c)10^13-10^14 cm^-3
1×10^14
5×10^13
2×10^13
1×10^13
Line intensity ratio R^eff(492.2 nm / 471.3 nm)
Electron temperature T_e [eV]

Fig. B4

Recent Issues of NIFS Series

NIFS-302 K. Nishimura, R. Kumazawa, T. Mutoh, T. Watari, T. Seki, A. Ando, S. Masuda, F. Shinpo, S. Murakami, S. Okamura, H. Yamada, K. Matsuoka, S. Morita, T. Ozaki, K. Ida, H. Iguchi, I. Yamada, A. Ejiri, H. Idei, S. Muto, K. Tanaka, J. Xu, R. Akiyama, H. Arimoto, M. Isobe, M. Iwase, O. Kaneko, S. Kubo, T. Kawamoto, A. Lazaros, T. Morisaki, S. Sakakibara, Y. Takita, C. Takahashi and K. Tsumori,
ICRF Heating in CHS; Sep. 1994 (IAEA-CN-60/A-6-I-4)

NIFS-303 S. Okamura, K. Matsuoka, K. Nishimura, K. Tsumori, R. Akiyama, S. Sakakibara, H. Yamada, S. Morita, T. Morisaki, N. Nakajima, K. Tanaka, J. Xu, K. Ida, H. Iguchi, A. Lazaros, T. Ozaki, H. Arimoto, A. Ejiri, M. Fujiwara, H. Idei, A. Iiyoshi, O, Kaneko, K. Kawahata, T. Kawamoto, S. Kubo, T. Kuroda, O. Motojima, V.D. Pustovitov, A. Sagara, C. Takahashi, K. Toi and I. Yamada,
High Beta Experiments in CHS; Sep. 1994 (IAEA-CN-60/A-2-IV-3)

NIFS-304 K. Ida, H. Idei, H. Sanuki, K. Itoh, J. Xu, S. Hidekuma, K. Kondo, A. Sahara, H. Zushi, S.-I. Itoh, A. Fukuyama, K. Adati, R. Akiyama, S. Bessho, A. Ejiri, A. Fujisawa, M. Fujiwara, Y. Hamada, S. Hirokura, H. Iguchi, O. Kaneko, K. Kawahata, Y. Kawasumi, M. Kojima, S. Kubo, H. Kuramoto, A. Lazaros, R. Liang, K. Matsuoka, T. Minami, T. Mizuuchi, T. Morisaki, S. Morita, K. Nagasaki, K. Narihara, K. Nishimura, A. Nishizawa, T. Obiki, H. Okada, S. Okamura, T. Ozaki, S. Sakakibara, H. Sakakita, A. Sagara, F. Sano, M. Sasao, K. Sato, K.N. Sato, T. Saeki, S. Sudo, C. Takahashi, K. Tanaka, K. Tsumori, H.Yamada, I. Yamada, Y. Takita, T. Tuzuki, K. Toi and T. Watari,
Control of Radial Electric Field in Torus Plasma; Sep. 1994
(IAEA-CN-60/A-2-IV-2)

NIFS-305 T. Hayashi, T. Sato, N. Nakajima, K. Ichiguchi, P. Merkel, J. Nührenberg, U. Schwenn, H. Gardner, A. Bhattacharjee and C.C.Hegna,
Behavior of Magnetic Islands in 3D MHD Equilibria of Helical Devices;
Sep. 1994 (IAEA-CN-60/D-2-II-4)

NIFS-306 S. Murakami, M. Okamoto, N. Nakajima, K.Y. Watanabe, T. Watari, T. Mutoh, R. Kumazawa and T. Seki,
Monte Carlo Simulation for ICRF Heating in Heliotron/Torsatrons;
Sep. 1994 (IAEA-CN-60/D-P-I-14)

NIFS-307 Y. Takeiri, A. Ando, O. Kaneko, Y. Oka, K. Tsumori, R. Akiyama, E. Asano, T. Kawamoto, T. Kuroda, M. Tanaka and H. Kawakami,
Development of an Intense Negative Hydrogen Ion Source with a Wide-Range of External Magnetic Filter Field; Sep. 1994

NIFS-308 T. Hayashi, T. Sato, H.J. Gardner and J.D. Meiss,
Evolution of Magnetic Islands in a Heliac; Sep. 1994

NIFS-309 H. Amo, T. Sato and A. Kageyama,
Intermittent Energy Bursts and Recurrent Topological Change of a Twisting Magnetic Flux Tube; Sep.1994

NIFS-310 T. Yamagishi and H. Sanuki,
Effect of Anomalous Plasma Transport on Radial Electric Field in Torsatron/Heliotron; Sep. 1994

NIFS-311 K. Watanabe, T. Sato and Y. Nakayama,
Current-profile Flattening and Hot Core Shift due to the Nonlinear Development of Resistive Kink Mode; Oct. 1994

NIFS-312 M. Salimullah, B. Dasgupta, K. Watanabe and T. Sato,
Modification and Damping of Alfvén Waves in a Magnetized Dusty Plasma; Oct. 1994

NIFS-313 K. Ida, Y. Miura, S -I. Itoh, J.V. Hofmann, A. Fukuyama, S. Hidekuma, H. Sanuki, H. Idei, H. Yamada, H. Iguchi, K. Itoh,
Physical Mechanism Determining the Radial Electric Field and its Radial Structure in a Toroidal Plasma; Oct. 1994

NIFS-314 Shao-ping Zhu, R. Horiuchi, T. Sato and The Complexity Simulation Group,
Non-Taylor Magnetohydrodynamic Self-Organization; Oct. 1994

NIFS-315 M. Tanaka,
Collisionless Magnetic Reconnection Associated with Coalescence of Flux Bundles; Nov. 1994

NIFS-316 M. Tanaka,
Macro-EM Particle Simulation Method and A Study of Collisionless Magnetic Reconnection; Nov. 1994

NIFS-317 A. Fujisawa, H. Iguchi, M. Sasao and Y. Hamada,
Second Order Focusing Property of 210° Cylindrical Energy Analyzer; Nov. 1994

NIFS-318 T. Sato and Complexity Simulation Group,
Complexity in Plasma - A Grand View of Self- Organization; Nov. 1994

NIFS-319 Y. Todo, T. Sato, K. Watanabe, T.H. Watanabe and R. Horiuchi,
MHD-Vlasov Simulation of the Toroidal Alfvén Eigenmode; Nov. 1994

NIFS-320 A. Kageyama, T. Sato and The Complexity Simulation Group,
Computer Simulation of a Magnetohydrodynamic Dynamo II: Nov. 1994

NIFS-321 A. Bhattacharjee, T. Hayashi, C.C.Hegna, N. Nakajima and T. Sato,
Theory of Pressure-induced Islands and Self-healing in Three-

dimensional Toroidal Magnetohydrodynamic Equilibria; Nov. 1994

NIFS-322 A. Iiyoshi, K. Yamazaki and the LHD Group,
Recent Studies of the Large Helical Device; Nov. 1994

NIFS-323 A. Iiyoshi and K. Yamazaki,
The Next Large Helical Devices; Nov. 1994

NIFS-324 V.D. Pustovitov
Quasisymmetry Equations for Conventional Stellarators; Nov. 1994

NIFS-325 A. Taniike, M. Sasao, Y. Hamada, J. Fujita, M. Wada,
The Energy Broadening Resulting from Electron Stripping Process of a Low Energy Au^- Beam; Dec. 1994

NIFS-326 I. Viniar and S. Sudo,
New Pellet Production and Acceleration Technologies for High Speed Pellet Injection System "HIPEL" in Large Helical Device; Dec. 1994

NIFS-327 Y. Hamada, A. Nishizawa, Y. Kawasumi, K. Kawahata, K. Itoh, A. Ejiri, K. Toi, K. Narihara, K. Sato, T. Seki, H. Iguchi, A. Fujisawa, K. Adachi, S. Hidekuma, S. Hirokura, K. Ida, M. Kojima, J. Koong, R. Kumazawa, H. Kuramoto, R. Liang, T. Minami, H. Sakakita, M. Sasao, K.N. Sato, T. Tsuzuki, J. Xu, I. Yamada, T. Watari,
Fast Potential Change in Sawteeth in JIPP T-IIU Tokamak Plasmas; Dec. 1994

NIFS-328 V.D. Pustovitov,
Effect of Satellite Helical Harmonics on the Stellarator Configuration; Dec. 1994

NIFS-329 K. Itoh, S-I. Itoh and A. Fukuyama,
A Model of Sawtooth Based on the Transport Catastrophe; Dec. 1994

NIFS-330 K. Nagasaki, A. Ejiri,
Launching Conditions for Electron Cyclotron Heating in a Sheared Magnetic Field; Jan. 1995

NIFS-331 T.H. Watanabe, Y. Todo, R. Horiuchi, K. Watanabe, T. Sato,
An Advanced Electrostatic Particle Simulation Algorithm for Implicit Time Integration; Jan. 1995

NIFS-332 N. Bekki and T. Karakisawa,
Bifurcations from Periodic Solution in a Simplified Model of Two-dimensional Magnetoconvection; Jan. 1995

NIFS-333 K. Itoh, S.-I. Itoh, M. Yagi, A. Fukuyama,
Theory of Anomalous Transport in Reverse Field Pinch; Jan. 1995

NIFS-334 K. Nagasaki, A. Isayama and A. Ejiri
Application of Grating Polarizer to 106.4GHz ECH System on Heliotron-E; Jan. 1995

NIFS-335 H. Takamaru, T. Sato, R. Horiuchi, K. Watanabe and Complexity Simulation Group,
A Self-Consistent Open Boundary Model for Particle Simulation in Plasmas; Feb. 1995

NIFS-336 B.B. Kadomtsev,
Quantum Telegragh : is it possible?; Feb. 1995

NIFS-337 B.B.Kadomtsev,
Ball Lightning as Self-Organization Phenomenon; Feb. 1995

NIFS-338 Y. Takeiri, A. Ando, O. Kaneko, Y. Oka, K. Tsumori, R. Akiyama, E. Asano, T. Kawamoto, M. Tanaka and T. Kuroda,
High-Energy Acceleration of an Intense Negative Ion Beam; Feb. 1995

NIFS-339 K. Toi, T. Morisaki, S. Sakakibara, S. Ohdachi, T.Minami, S. Morita, H. Yamada, K. Tanaka, K. Ida, S. Okamura, A. Ejiri, H. Iguchi, K. Nishimura, K. Matsuoka, A. Ando, J. Xu, I. Yamada, K. Narihara, R. Akiyama, H. Idei, S. Kubo, T. Ozaki, C. Takahashi, K. Tsumori,
H-Mode Study in CHS; Feb. 1995

NIFS-340 T. Okada and H. Tazawa,
Filamentation Instability in a Light Ion Beam-plasma System with External Magnetic Field; Feb. 1995

NIFS-341 T. Watanbe, G. Gnudi,
A New Algorithm for Differential-Algebraic Equations Based on HIDM; Feb. 13, 1995

NIFS-342 Y. Nejoh,
New Stationary Solutions of the Nonlinear Drift Wave Equation; Feb. 1995

NIFS-343 A. Ejiri, S. Sakakibara and K. Kawahata,
Signal Based Mixing Analysis for the Magnetohydrodynamic Mode Reconstruction from Homodyne Microwave Reflectometry; Mar.. 1995

NIFS-344 B.B.Kadomtsev, K. Itoh, S.-I. Itoh
Fast Change in Core Transport after L-H Transition; Mar. 1995

NIFS-345 W.X. Wang, M. Okamoto, N. Nakajima and S. Murakami,
An Accurate Nonlinear Monte Carlo Collision Operator; Mar. 1995